HHS Public Access

Author manuscript

Nat Cell Biol. Author manuscript; available in PMC 2018 December 25.

Published in final edited form as:

Nat Cell Biol. 2018 July ; 20(7): 811–822. doi:10.1038/s41556-018-0122-3.

Mutant GNAS drives pancreatic tumorigenesis by inducing PKA-mediated SIK suppression and reprogramming lipid metabolism

Krushna C. Patra[1,5], **Yasutaka Kato**[1], **Yusuke Mizukami**[1,9,*], **Sebastian Widholz**[1], **Myriam Boukhali**[1], **Iulia Revenco**[1], **Elizabeth A. Grossman**[10], **Fei Ji**[4,8], **Ruslan I. Sadreyev**[1,2,6], **Andrew S. Liss**[1], **Robert A. Screaton**[11], **Kei Sakamoto**[12,^], **David P. Ryan**[1,5], **Mari Mino-Kenudson**[1,2,6], **Carlos Fernandez-del Castillo**[1,3,7], **Daniel K. Nomura**[10], **Wilhelm Haas**[1], and **Nabeel Bardeesy**[1,5]

[1]Center for Cancer Research

[2]Department of Pathology

[3]Department of Surgery

[4]Department of Molecular Biology, Massachusetts General Hospital, Boston, MA 02114, USA

[5]Departments of Medicine

[6]Department of Pathology

[7]Department of Surgery

[8]Department of Genetics, Harvard Medical School, Boston, MA 02115 USA

[9]Institute of Biomedical Research, Sapporo Higashi Tokushukai Hospital, Sapporo, Hokkaido 065-0033, JAPAN

[10]Departments of Nutritional Sciences and Toxicology, Chemistry, and Molecular and Cell Biology, University of California, Berkeley, CA 94720 USA

[11]Sunnybrook Research Institute, Toronto, Canada, M4N 3M5, Dept. of Biochemistry, University of Toronto, Toronto, Canada, M5S 1A8

[12]MRC Protein Phosphorylation and Ubiquitylation Unit, School of Life Sciences, University of Dundee, Scotland, UK

Bardeesy.Nabeel@mgh.harvard.edu; Phone: 617-643-2579; Fax: 617-643-3170.

*Present Address: Asahikawa Medical University, Hokkaido, Japan

^Present Address: Nestlé Institute of Health Sciences SA, Lausanne, Switzerland

Conflicts of Interest: No conflicts to disclose

Author Contributions

K.C.P., Y.M., and N.B conceived and designed the study. Y.M. generated the TetO-GNAS^{R201C} mouse strain. K.P. performed most of the animal and cell-based experiments, with assistance of Y.K., Y.M., S.W., and I.R. Y.K. and M.M-K performed histological analysis. M.B. and W.H. performed proteomics analysis and interpreted the data. F.J. and R.I.S. performed bioinformatics analysis. E.A.G. did LC-MS for polar metabolites, and D.K.N. analysed and interpreted the data. A.S.L., R.A.S., and K.S. provided essential resources. A.S.L., R.A.S., K.S., D.P.R. M.M-K. and C.F.C provided important intellectual input and data interpretation. K.C.P. and N.B. wrote the manuscript with feedback from all authors. N.B. supervised the studies.

Abstract

G-protein α_s (GNAS) mediates receptor-stimulated cAMP signaling, which integrates diverse environmental cues with intracellular responses. GNAS is mutationally activated in multiple tumor types, although its oncogenic mechanisms remain elusive. We explored this question in pancreatic tumorigenesis where concurrent *GNAS* and *KRAS* mutations characterize pancreatic ductal adenocarcinomas (PDAs) arising from Intraductal Papillary Mucinous Neoplasms (IPMNs). By developing genetically engineered mouse models, we show that $GNAS^{R201C}$ cooperates with $KRAS^{G12D}$ to promote initiation of IPMN, which progress to invasive PDA following Tp53 loss. Mutant-GNAS remains critical for tumor maintenance in vivo. This is driven by protein kinase A-mediated suppression of salt-inducible kinases (SIK1-3), associated with induction lipid remodeling and fatty acid oxidation. Comparison of *KRAS*-mutant pancreatic cancer cells with and without *GNAS* mutations reveals striking differences in the functions of this network. Thus, we uncover GNAS-driven oncogenic mechanisms, identify SIKs as potent tumor suppressors, and demonstrate unanticipated metabolic heterogeneity among *KRAS*-mutant pancreatic neoplasms.

Keywords

pancreatic cancer; IPMN; cancer metabolism; GNAS; PKA; KRAS

GNAS encodes the $G\alpha_s$ stimulatory subunit of heterotrimeric G-proteins, which mediate G-protein-coupled receptor (GPCR) signaling, a central mechanism by which cells sense and respond to extracellular stimuli[1]. Ligand stimulation of GPCRs promotes GDP for GTP exchange on $G\alpha_s$, enabling $G\alpha_s$ to engage effectors. The primary target is adenylyl cyclase, which generates the second messenger, cAMP, an activator of protein kinase A (PKA), cyclic nucleotide-gated ion channels, and EPAC1/2 guanine-nucleotide exchange factors, although GNAS has reported cAMP-independent functions[2,3]. In many tissues, GNAS-cAMP signaling maintains quiescence or cellular differentiation[4–8]. However, multiple human cancer types exhibit recurrent gain-of-function mutations in the pathway, most frequently targeting *GNAS*[1]. These context-specific oncogenic functions are not well understood. Additionally, activating *GNAS* mutations often co-exist with driver mutations in *KRAS*[9–13] (ref.[13] accessed from www.cbioportal.org), thus it is uncertain whether mutant-*GNAS* remains important for the growth of tumors once they are established[14]. *GNAS* mutations and amplifications are particularly common in pancreatic tumorigenesis where their presence distinguishes two major precursors of invasive PDA; pancreatic intraepithelial neoplasias (PanINs) and IPMNs both exhibit frequent *KRAS* mutations, whereas *GNAS* mutations are exclusive to IPMN (present in ~41–75% of IPMNs[9,10,15] and ~2–11% of total PDAs[11,12,15,16]).

Results

Pancreas-specific $GNAS^{R201C}$ and $KRAS^{G12D}$ mutations cooperate to promote IPMNs

To examine the functions of mutationally activated GNAS in the murine pancreas and its cooperative interactions with oncogenic-KRAS, we generated a knock-in strain expressing $GNAS^{R201C}$ controlled by a doxycycline (Dox)-inducible promoter (*TetO-GNAS*^{R201C}) and crossed these mice with the *Ptf1a-Cre, Rosa26-LSL-rtTA,* and *LSL-KRAS*^{G12D} strains, to

establish GC (GNAS^{R201C};Cre), KC (KRAS^{G12D};Cre), and KGC (KRAS^{G12D};GNAS^{R201C};Cre) cohorts (Fig. 1a). KGC mice rapidly developed cystic pancreatic tumors requiring euthanasia (mean 9.7 weeks) (Fig. 1b–e). At this time point, KC mice had only focal PanINs[17] and GC mice had no abnormalities (Fig. 1c, d and Supplementary Fig. 1a). Histologic and immunostaining analyses of KGC tumors suggested equivalence to human gastric- and pancreatobiliary-type IPMN, with positive staining for Cytokeratin-19, Muc5AC and Muc1, but not Muc2 or Cdx2 (Fig. 1d and Supplementary Fig. 1b)[18]. Long-term monitoring revealed eventual development of invasive PDA in KC mice and low-grade IPMN in GC mice (mean survival 61 and 106 weeks, respectively) (Fig. 1b, f, g).

Serial analyses of KGC mice following Dox-mediated induction of GNAS^{R201C} revealed neoplastic lesions with ductal morphology within one week, which increased in size and number to encompass the entire organ after 3–7 weeks (Fig. 1e). The lesions exhibited staged histological progression, gradually acquiring papillary architecture, nuclear stratification, and atypical nuclei. Collectively, these studies show that GNAS^{R201C} alone is weakly oncogenic in the pancreas, but potently synergizes with KRAS^{G12D}, shifting the PanIN phenotype to that resembling high-grade IPMN and accelerating tumorigenesis.

Tp53 loss facilitates progression of KRAS/GNAS-mutant IPMN to invasive PDA

Consistent with the clinical behavior of most human IPMNs, we did not observe invasion in KGC mice despite the presence of high-grade dysplasia (Supplementary Fig. 1c). *TP53* mutations arise as a late event in advanced human IPMNs and co-exist with *GNAS* mutations in a subset of PDA[10,12,13,16] (ref.[13] accessed from www.cbioportal.org), prompting us to examine the impact of this genetic alteration. To this end, we generated mice with combinations of conditional heterozygous *KRAS^{G12D}*, *GNAS^{R201C}*, and *Tp53^{LoxP}* alleles. KGC mice exhibit rapid onset of end-stage disease due to extensive IPMN burden; therefore, we used the *Ptf1a-Cre^{ER}* system to recombine the mutant alleles more focally in adult pancreatic acinar cells (Fig. 2a). Notably, KGPC^{ER} mice (KRAS^{G12D}; GNAS^{R201C}; p53$^{LoxP/+}$; Cre^{ER}) developed malignant ascites and invasive tumors with significantly shorter latency compared to KPC^{ER} (KRAS^{G12D}; p53$^{LoxP/+}$; Cre^{ER}) animals (KGPC^{ER}: mean 25.8 weeks; KPC^{ER}: mean 38.3 weeks); invasive disease was never observed in the other cohorts. Histological analysis of end-stage KGPC^{ER} mice revealed PDAs contiguous with high-grade IPMNs and showing liver and peritoneal dissemination, whereas age-matched KGC^{ER} and KPC^{ER} mice had only IPMNs and PanINs, respectively (KGPC^{ER} and KGC^{ER}, N=8 mice/group; KPC^{ER}, N=5 mice) (Fig. 2b–d). Loss of wild-type *Tp53* was observed in 3 of 4 KGPC^{ER} PDAs (Fig. 2e). To extend these data, we tested directly whether *Tp53* inactivation enables IPMN-to-PDA progression utilizing primary cultures established from KGC tumors. Orthotopic injection of parental KGC^{Control} cells into SCID mice resulted in non-invasive IPMNs, recapitulating the phenotype of the autochthonous KGC model, whereas shRNA-mediated knockdown of *Tp53* (KGC^{shp53} cells) resulted in invasive PDA (Fig. 2f, g). Thus, IPMNs harboring hallmark *GNAS* and *KRAS* mutations can progress to PDA, and *Tp53* is an important barrier to the onset of malignancy.

GNAS^{R201C} is critical for pancreatic tumor maintenance

The circuits supporting the growth of established IPMNs and resulting PDA have yet to be defined. Our Dox-inducible system enabled us to investigate whether GNAS^{R201C} is required for tumor maintenance. To this end, KGC animals were provided Dox until palpable tumors were present, and then Dox was withdrawn (Fig. 3a, Dox-Off group). These mice showed immediate improvements in body condition, including reductions in abdominal size and cyst fluid (Fig. 3b and Supplementary Fig. 2a). Remarkably, they remained healthy for >20 weeks, whereas the Dox-On group required euthanasia within 1–3 weeks of tumor detection (Fig. 3c). Serial analyses of tumors following Dox withdrawal revealed rapid loss of dysplastic papillary features, reduced mucins, and decreased proliferation (Fig. 3d), without evidence of apoptosis (Supplementary Fig. 2b). Furthermore, organoids derived from KGC IPMNs and KGPC^{ER} PDAs remained dependent on GNAS^{R201C} for tumor formation and maintenance, as assessed by injection into SCID mice ± Dox supplementation and by acute Dox withdrawal following tumor establishment, respectively (Fig. 3e–g). Thus, GNAS^{R201C} is critical for sustained pancreatic tumor growth, despite the presence of concurrent KRAS and p53 mutations. This tumor maintenance function and induction of PDA from IPMNs rather than PanINs suggest that mutant-GNAS may establish a unique molecular program in PDA distinct from that resulting from KRAS/p53 mutations alone.

GNAS^{R201C} supports pancreatic tumor growth via cAMP-PKA signaling

We used tumor-derived organoids from the KGC (IPMN) and KGC^{shp53} (PDA) models to define the oncogenic mechanisms of GNAS^{R201C}. Dox withdrawal abrogated organoid growth *in vitro*, indicating that GNAS^{R201C}-driven tumor maintenance involves cell-intrinsic mechanisms. GNAS^{R201C} extinction led to a decrease in cAMP whereas treatment with the adenylyl cyclase agonist, forskolin (FSK), boosted cAMP levels and rescued organoid growth (Fig. 4a–d and Supplementary Fig. 3a–c). These data are consistent with a primary role for adenylyl cyclase/cAMP signaling downstream of GNAS^{R201C}, rather than engagement of non-canonical targets[3,19]. cAMP activates multiple effectors (Fig. 4c), including PKA, whose subunits are abundantly expressed in KGC cultures, and EPAC1/2, which are virtually undetectable (Supplementary Fig. 3d). Accordingly, activation of PKA with the cAMP analog, 8- Bromoadenosine- 3′, 5′-cyclic monophosphorothioate, Sp-isomer, acetoxymethyl ester (Sp-8-Br-cAMPS) rescued colony formation, whereas the EPAC-specific agonist, 8-(4-Chlorophenylthio)- 2′-O-methyladenosine- 3′, 5′-cyclic monophosphate (8-pCPT-2′-O-Me-cAMP) had no effect (Fig. 4d; PKA activation by FSK and Sp-8-Br-cAMPs is shown in Supplementary Fig. 3e). Moreover, GNAS^{R201C} extinction decreased PKA signaling *in vitro* and *in vivo* as reflected by phosphorylation of VASP and proteins detected with phospho-PKA substrate antibody (Fig. 4e, f, Supplementary Fig. 3g; Dox-dependent regulation of GNAS expression *in vivo* is shown in Supplementary Fig. 3f, g). Correspondingly, ectopic expression of a dominant-negative PKA mutant (PKA^{DN}) attenuated growth of KGC and KGC^{shp53} organoids *in vitro* and suppressed tumorigenesis upon organoid injection *in vivo* (Fig. 4g–i and Supplementary Fig. 3h, i); inhibition of PKA signaling by PKA^{DN} is shown in Fig. 5c). These experiments establish PKA as a principal effector of oncogenic GNAS^{R201C}.

The SIK kinases are critical targets of oncogenic GNAS-PKA signaling in pancreatic tumors

CREB, the classic PKA substrate, and several other direct or indirect PKA targets implicated in growth control either showed no phosphorylation changes (CREB, YAP, β-catenin) or increased activating phosphorylation (ERK1/2) upon $GNAS^{R201C}$ silencing (Supplementary Fig. 4a)[20–22]. A broader network by which PKA integrates responses to hormonal cues involves phosphorylation of Salt-Inducible Kinases (SIK1, 2, and 3), which prevents SIKs from phosphorylating key substrates[21] (Fig. 5a). Like cAMP/PKA signaling, SIKs have context-dependent tumor-promoting and -suppressing roles[23–25]. Consistent with $GNAS^{R201C}$-mediated control of this pathway in KGC cells, Dox withdrawal reduced SIK2 phosphorylation at each documented PKA site (Fig. 5b)[26,27]. Accordingly, there was increased phosphorylation of established SIK targets, CRTC2-S171, CRTC2-S275 and HDAC7-S155 (Fig. 5b)[21,26]. PKA^{DN} expression recapitulated these effects (Fig. 5c). Thus, oncogenic $GNAS^{R201C}$-PKA signaling leads to sustained inhibition of SIK kinases in pancreatic tumor cells.

SIK1-3 have overlapping functions and each is readily detectable in *GNAS*-mutant organoids (SIK2 and 3 are visualized by immunoblot with available antibodies whereas SIK1 is not, but has highest mRNA levels; Fig. 5f and Supplementary Fig. 4b). This prompted us to study their roles as a group using small molecule pan-SIK inhibitors (HG-9-91-01 and KIN-112)[26,28]. Remarkably, these compounds rescued proliferation of KGC organoids following $GNAS^{R201C}$ silencing, with effects proportional to the extent of SIK inhibition gauged by CRTC2 phosphorylation (Fig. 5d, e). Conversely, expression of the SIK2-S4A mutant[26,27], which is resistant to cAMP/PKA-dependent phosphorylation, strongly suppressed growth of KGC organoids compared to WT-SIK2 (Supplementary Fig. 4c). We corroborated these studies with CRISPR-mediated gene editing using two independent sets of sgRNAs to knock out SIK1-3 in KGC cells. qRT-PCR and immunoblot confirmed that $SIK1\text{-}3^{KO}$ cells lost *Sik1-3* expression and lacked induction of CRTC2 phosphorylation upon Dox withdrawal (Supplementary Fig. 4d and Fig. 5f). Importantly, $SIK1\text{-}3^{KO}$ rescued both organoid growth *in vitro* and subcutaneous tumor growth following $GNAS^{R201C}$ silencing (Fig. 5g, h). Thus, the cAMP-PKA-SIK axis is critical for $GNAS^{R201C}$-driven tumor growth.

To test this circuit in human PDA, we generated a cell line (950-5-BLK) from a human PDA harboring $KRAS^{G12V}$, $GNAS^{R201H}$ and $TP53^{R273C}$ mutations (Fig. 6A) and compared this model with a series of KRAS-mutant/$GNAS^{WT}$ patient-derived and established PDA cell lines. Immunoblot analysis revealed that 950-5-BLK cells had high relative levels of phospho-PKA substrates and phospho-VASP and low phospho:total CRTC2 levels, consistent with constitutive PKA activity and impaired SIK function (Fig. 6b). Moreover, shRNA-mediated knockdown of GNAS promoted SIK activity specifically in 950-5-BLK cells, as reflected by increased CRTC2 phosphorylation (Fig. 6c). Ectopic expression of PKA^{DN} also increased CRTC phosphorylation in 950-5-BLK cells (Fig. 6e). Importantly, PKA^{DN} inhibited the growth of 950-5-BLK tumor spheres and subcutaneous xenografts, while having minimal effects in three human GNAS-WT PDA models (Fig. 6d–f). Moreover, SIK inhibitors rescued growth of PKA^{DN} expressing organoids (Fig. 6g).

Therefore, oncogenic GNAS-PKA-SIK signaling is a conserved mechanism of murine and human pancreatic tumor maintenance.

Mutant GNAS reprograms lipid metabolism in pancreatic tumor cells

The GNAS-PKA-SIK pathway modulates lipolysis and lipid synthesis in liver and adipose tissue[29–32]. Notably, global quantitative proteomics of KGC tumor organoids ± Dox and Gene Set Enrichment Analysis (GSEA) revealed enrichment of processes relating to lipid metabolism and in components of the peroxisome (microbody), an organelle required for processing of very long-chain fatty acids and generation of ether lipids[33,34] (Fig. 7a, Supplementary Fig. 5a). qRT-PCR following Dox removal or treatment with the PKA inhibitor, KT5720, indicate that $GNAS^{R201C}$-PKA signaling supports the transcription of multiple lipid metabolism enzymes (Supplementary Fig. 5b). Comparable expression changes were observed upon acute $GNAS^{R201C}$ silencing in subcutaneous KGC tumors *in vivo* (Supplementary Fig. 5c). Moreover, PKA^{DN} caused similar expression changes in human GNAS-mutant 950-5-BLK cells, while not significantly affecting GNAS-WT PDA models (Supplementary Fig. 5d).

Based on these observations and the central role of GNAS-PKA-SIK signaling in regulating lipid metabolism in normal tissues[21,29–31,35], we examined the potential functions of oncogenic $GNAS^{R201C}$ in reprogramming tumor cell metabolism. Free fatty acids synthesized *de novo* or imported into the cell are rapidly esterified to glycerolipids/triglycerides (TG)[29,36–38]. Thus, complementary lipolytic processes are required to provide fatty acid substrates for signaling, structural, and metabolic purposes, and recent studies have shown that various oncogenes coordinate this lipid network in different tumor types[29,38–40]. Using BODIPY staining and lipidomic profiling of KGC organoids, we found that $GNAS^{R201C}$ inactivation caused a decrease in total lipids including TG, as well as specific depletion of several lipid classes (Supplementary Fig. 6a–c). There was a particularly pronounced reduction in ether lipids, in keeping with the downregulation of the ether lipid biosynthesis enzymes, Far1 and Agps (Supplementary Fig. 5b, c and 6d, e). However, the ratio of monoglycerides/triglycerides (MG:TG) and monoglycerides/diglycerides (MG:DG) was decreased following Dox withdrawal (Fig. 7b), suggesting that $GNAS^{R201C}$ promotes lipid hydrolysis in addition to lipid synthesis and remodeling.

In KRAS-mutant pancreatic cancers lacking GNAS mutations, both lipid accumulation and fatty acid oxidation (FAO) are restricted by KRAS signaling[41]. By contrast, our data indicate that these processes are activated by $GNAS^{R201C}$ (despite concurrent $KRAS^{G12D}$ mutations), prompting us to examine lipid metabolism in further detail. In adipocytes, the GNAS-PKA-SIK axis controls lipolysis through PKA-mediated phosphorylation events as well as SIK-dependent transcriptional changes[21,29–31,38]. Accordingly, $GNAS^{R201C}$ extinction in KGC organoids led to loss of activating phosphorylation (Ser-660) of hormone-sensitive lipase (HSL) (Fig. 7c) and reduced expression of other lipases (Supplementary Fig. 5b–d and Supplementary Fig. 6f). Reduced phospho-HSL was also observed upon Dox withdrawal in established tumors *in vivo* (Supplementary Fig. 6h). Fatty acids taken up by the cell, synthesized, or derived from lipolysis can be broken down through FAO, a process in which PKA has also been implicated[42–44]. Correspondingly, assessment of CO_2 release

from ^{14}C-labelled oleate in KGC cultures ± Dox demonstrated that GNAS^{R201C} was required to sustain FAO activity (Fig. 7d). The use of PKA^{DN} confirmed that this effect was PKA-dependent (Fig. 7e). PKA^{DN} also suppressed FAO in human GNAS-mutant (950-5-BLK) but not GNAS-WT PDA cells (Supplementary Fig. 6g). Importantly, FSK or SIK inhibitor treatment or SIK1-3^{KO} rescued FAO following GNAS^{R201C} extinction (Supplementary Fig. 6i, j). Thus, GNAS^{R201C} activates multiple aspects of lipid metabolism including potentiating FAO through the PKA-SIK axis.

LC-MS/MS-based profiling of 95 polar metabolites spanning central metabolic pathways revealed that GNAS^{R201C} silencing in KGC cells led to a decrease in acetyl-CoA (Fig. 7f), which is a main product of FAO. Moreover, shRNA-mediated silencing of Carnitine palmitoyltransferase 1a (Cpt1a), the rate-limiting enzyme for fatty acid transport into mitochondria, reduced acetyl-CoA levels in KGC organoids but not in GNAS^{WT} PDA organoids from a *KRAS*-mutant/Tp53-deficient genetically engineered mouse model (GEMM) (Supplementary Fig. 6k). These data suggest that FAO supports acetyl-CoA levels in these tumor cells.

Metabolic reprogramming is a hallmark of PDA driven by oncogenic KRAS and involves enhanced glycolysis and attenuated FAO[41,45]. Our studies indicated that GNAS^{R201C} induces a distinct set of metabolic processes, suggesting that there may be differences in the circuitry of KRAS-mutant pancreatic tumors depending on GNAS mutational status. Notably, comparison of four independently-derived lines per group of murine GNAS-mutant and GNAS^{WT} PDA organoids revealed opposite patterns of PKA and SIK activity (Fig. 7g), consistent with observations in human PDA cells (Fig. 6b). Moreover, FSK treatment compromised the growth of multiple *GNAS*^{WT} PDA organoids while promoting that of GNAS-mutant organoids (Fig. 7h). Conversely, *GNAS*-mutant organoids were highly sensitive to PKA^{DN} expression (Fig. 4h, above) or treatment with the PKA inhibitor, KT5720, while *GNAS*^{WT} PDA organoids were largely unaffected (Supplementary Fig. 7a, b). Thus, the biological effects and activation state of the cAMP-PKA-SIK pathway distinguishes these subsets of *KRAS*-mutant pancreatic tumors.

Notably, GNAS^{R201C}-expressing cells had a greater FAO rate relative to *GNAS*^{WT} cells (Fig. 7i and Supplementary Fig. 7c). Furthermore, GNAS-mutant organoids were specifically responsive to inhibition of lipid degradation, using the lipase/carboxyesterase inhibitor, WWL113[46] (Supplementary Fig. 7d), and showed preferential sensitivity to FAO inhibition by Cpt1a knockdown or treatment with the FAO inhibitor, 4-bromocrotonic acid (BrCA) (Fig. 7j and Supplementary Fig. 7e, f). Cpt1a knockdown also impaired tumorigenicity *in vivo* (Fig. 7k). By contrast, GNAS-mutant and GNAS^{WT} organoids responded similarly to glycolysis inhibition using 2-deoxyglucose (2DG) or oxamate, indicating that *GNAS*-mutant pancreatic cancer cells do not exhibit general increased vulnerability to metabolic stress and reinforcing the specificity of the observed responses to inhibition of lipid metabolism (Supplementary Fig. 7g, h).

Discussion

The oncogenic functions of GNAS remain under-investigated despite increasing evidence for its mutational activation in human tumors. Moreover, there is a critical need to understand the diversity of pancreatic cancer subtypes, including IPMN-associated tumors, which comprise ~10% of PDA [10,11,15,16,47]. By establishing an inducible GEM model that recapitulates the human IPMN-PDA sequence, we demonstrate that $GNAS^{R201C}$ cooperates with $KRAS^{G12D}$ and *Tp53* loss to drive tumor initiation and progression and has a persistent role in maintenance of advanced malignancy. This function is mediated by PKA-dependent inactivation of SIK1-3, establishing SIKs as critical tumor suppressors and suggesting the therapeutic potential of inhibition of GNAS-PKA signaling in GNAS-mutant pancreatic tumors. Comparison of $KRAS^{G12D}$-driven pancreatic tumor models defined opposing roles for the PKA-SIK pathway and distinct metabolic requirements depending on *GNAS* mutational status. Thus, KRAS-mutant pancreatic tumor cells have heterogeneous circuits for growth and nutrient utilization governed by their combinations of cooperating gene mutations.

Our studies reveal negative regulation of SIK kinases as a primary mechanism by which $GNAS^{R201C}$-PKA-drives pancreatic tumorigenesis. Whereas inactivating mutations of SIK kinases are infrequent in human cancers, perhaps reflecting redundancy, the mutant-GNAS-PKA pathway inhibits SIK1-3, thereby unmasking their tumor suppressor activity. Genetic alterations in pathways potentially converging on SIK signaling are found across several sporadic tumor types and include other instances of *GNAS* mutations, mutation of PKA subunits, and loss-of-function of *LKB1*/*STK11*, an activator of SIK kinases[1,48–50]. Moreover, genetic syndromes involving *GNAS* (McCune-Albright syndrome), *PKA* (Carney Complex), and *LKB1* (Peutz-Jeghers syndrome) have overlapping features including abnormal pigmentation and predisposition to a spectrum of tumors, including IPMN[51,52]. Thus, our findings suggest the possibility that SIK inactivation may comprise a common node contributing to these different diseases.

The GEM models provide insights into the natural history of IPMNs and their relationship to PanIN and PDA. $GNAS^{R201C}$ induction promotes IPMN with long latency and shows dramatic cooperation with $KRAS^{G12D}$, shifting $KRAS^{G12D}$-driven PanIN to more proliferative and dysplastic IPMN lesions (see also reference[53] reporting a non-inducible transgenic model of GNAS-/KRAS-mutant IPMN). Additionally, while prior studies have suggested that the distinct features of IPMN versus PanIN may reflect differing cells-of-origin (proposed to arise from ducts and acinar cells, respectively)[54], our observations using the Ptf1a-Cre^{ER} system show that acinar cells readily give rise to IPMNs (Fig. 2b), indicating that underlying mutations rather than cell-of-origin direct this neoplastic phenotype. Moreover, in humans, IPMNs often remain benign, and GNAS mutations are associated with relatively indolent tumors across several tissues, therefore, there is uncertainty regarding the relationship between IPMNs and PDA and the potential of mutant-GNAS to drive invasive tumor growth[14]. Consistent with having constrained malignant potential, GNAS/KRAS-mutant murine IPMNs did not typically progress to PDA. However, Tp53 deficiency in the $KGPC^{ER}$ model and acute Tp53 inactivation in KGC organoids

resulted in invasive PDA, revealing Tp53 as a central barrier for IPMN advancement and reinforcing the paradigm of direct IPMN-to-PDA progression (Fig. 2)[10].

Established murine KGC and KGCP tumors remained dependent on mutant-GNAS/PKA signaling for sustained growth. Our data in 950-5-BLK cultures and xenografts indicate that at least a subset of GNAS-mutant human PDA likely remain dependent on this pathway. The KGC tumors exhibit rapid and progressive responses to $GNAS^{R201C}$ inactivation (Fig. 3e–g). Within days of Dox withdrawal, cell proliferation, mucin expression, and dysplastic histologic features were reduced, followed by a gradual loss of papillary architecture (Fig. 3d). Unlike $KRAS^{G12D}$ extinction in the KPC model of PDA[45,55], there was no evidence of apoptosis (Supplementary Fig. 2). These observations highlight distinct modes of oncogene addiction whereby different activated oncogenes support the neoplastic state by variously controlling proliferation, survival, differentiation and/or tumor-stroma interactions.

Our data also link oncogenic GNAS signaling to regulation of lipid metabolism. Mutant-GNAS promoted both maintenance of triglyceride levels and supported lipid breakdown via FAO. Coordinated triglyceride synthesis and degradation have been observed in other tumor types[40,56–58], including subsets of lung cancers where mutant-KRAS induces lipid uptake, triglyceride production, and FAO[39]. We also present evidence that mutant-GNAS contributes to steady state levels of acetyl-CoA, the substrate for fatty acid synthesis, TCA cycle activity, and protein acetylation. Whereas, acetyl-CoA is primarily derived from glucose or acetate in many cancers[59], our data suggest that FAO may be an important contributor to acetyl-CoA pools in GNAS-mutant pancreatic tumors cells. Overall, our studies highlight the broad rewiring of lipid metabolism by $GNAS^{R201C}$, although fully deciphering the metabolic processes controlled by mutant-GNAS will require metabolic labeling analysis and assessment of how intracellular and extracellular nutrient sources are mobilized.

Finally, our studies illustrate the dichotomous oncogenic versus tumor suppressive functions of cAMP/PKA signaling. We show that in the context of common $KRAS^{G12D}$ ± Tp53 mutations the cAMP-PKA pathway has opposite effects on pancreatic tumor cell proliferation depending on GNAS mutational status. Thus, KRAS-mutant pancreatic tumors have heterogeneous circuits for growth and governed by their combinations of cooperating gene mutations. Since >30% of FDA-approved drugs target GPCRs and largely function as cAMP-PKA modulators[60], understanding the effects of cAMP on tumor growth may predict new treatment avenues repurposing these compounds.

Methods

Chemicals, drugs, supplements, and other materials

Laminin (23017-95), CyQUANT NF (C35006), bovine pituitary extract (13038-14), HBSS, RPMI, DMEM, DMEM:F12, penicillin-streptomycin, pyruvate solution, fetal bovine serum (FBS), BODIPY 493/503 (D3922), B-27™ Supplement (50X), serum free (17504044) were from Life Technologies; Recombinant Human FGF-basic (100-18B) from Peprotech; doxycycline hyclate (D9891), nicotinamide (N3376), dexamethasone (D4902), 2-deoxyglucose (D6134), Sodium oxamate (O2751), collagenase (C7657), glucose (G7528), tamoxifen (T5648), Sodium oleate (O7501), Bovine Serum Albumin (A7030), Alcian Blue

(B8438), Roche cOmplete, Mini, EDTA-free Protease Inhibitor Cocktail (11836170001), ROCK inhibitor: Y-27632 (SCM075) were from Sigma;, Forskolin (1099), IBMX (2845), KT5720 (1288), WWL113 (5259) were from Tocris; mouse EGF (354001), NuSerum IV (355104), ITS+ Premix (354352) and Matrigel (354234) were from Corning; dispase (165–859; Roche); Sp-8-Br-cAMPS (B002) and 8-pCPT-2′-O-Me-cAMP (C041) were from Biology Life Science Institute; Oleic acid-[1-^{14}C] was from Perkin-Elmer (NEC315070UC); 4-Bromocrotonic Acid (BrCA) (B2298) was from TCI America; iTaq universal SyBR Green Supermix (BIO-RAD), Protein Block (X0909; DAKO); MACH2 HRP-Polymer (HRP520H) and Betazoid DAB Chromogen Kit (BDB2004H) from Biocare Medical; HG-9-91-01 and KIN112 were kindly provided by Dr. Nathanael Gray.

Antibodies

Please see Nature Research Reporting Summary for information on antibodies used in this study.

Lentiviral and retroviral vectors

Lentiviruses and retroviruses were produced in 293T cells by standard protocols with the packaging plasmids (pCMV-dR8.91 or pCL-Eco and pMD2.G (VSVG). To generate the pLX303-Dominant negative PKA-HA (PKA^{DN}) vector, m7 pDN-PKA-GFP (Addgene plasmid # 16716) was sub-cloned into the vector, pLX303 (Addgene Plasmid #25897), using the Life Technologies Gateway system. pLenti6-SIK2-WT and p-Lenti6-SIK2-4A mutants were subcloned from pShuttle-CMV-GFP-SIK2-WT and pShuttle-CMV-GFP-SIK2-4xAAAA (S343/A; S358/A; T484/A; S587/A) (supplied by Dr. Kei Sakamoto) into a modified pLenti6-Blast vector. All final plasmids were sequence verified. Murine Tp53 was knocked down using the *miR-30*-based LMS sh-p53.1224 retroviral vector[61]. All other knockdowns were performed using pLKO-based lentiviral shRNA vectors from The RNAi Consortium (TRC) library (Broad Institute), and were purchased from Molecular Profiling Laboratory, MGH. The CRISPR guides against *Sik* 1, 2 and 3 were cloned into pLentiCRISPRV2 (Addgene # 52961). Information on the shRNA and gRNA targeting sequences are shown in Supplementary Table 1.

Animal studies—Mice were housed in pathogen-free animal facilities. All experiments were conducted under protocol 2005N000148 approved by the Subcommittee on Research Animal Care at Massachusetts General Hospital and comply with all regulations for the ethical conduct of research. Mice were maintained on a mixed 129SV/C57Bl/6 background. Data presented include both male and female mice. All mice included in the survival analysis were euthanized when criteria for disease burden were reached (including abdominal distension that impeded movement, loss of >15% of body weight, labored breathing, and/or abnormal posture). Mouse strains were obtained from Jackson Laboratories; Rosa26-LSL-rtTA (#005572) and kindly provided by colleagues include Ptf1a-Cre[62] and Ptf1a-Cre^{ER} (#019378) mice from C. Wright, LSL-Kras^{G12D} (#008179) mice from D. Tuveson and T. Jacks, P53$^{Lox/Lox}$ (#008462) mice from A. Berns. To generate the doxycycline-inducible TetO-GNAS^{R201C} mouse strain (Fig. 1a), the GNAS^{R201C} mutation was introduced into the mouse Gnas cDNA (Harvard PlasmID, Clone: MmCD00314350, NCBI RefSeq accession number BC038067 or NM_201616.2) using the Quickchange kit

(Agilent Lexington, MA #200521) according to the manufacturer's instructions. The $GNAS^{R201C}$ cDNA was then cloned into the pBS31 Prime transgenic targeting vector (Thermo Scientific Open Biosystems, #MES4487). The targeting vector was co-electroporated into C2 mouse embryonic stem cells (Thermo Scientific Open Biosystems, #MES4305) with a plasmid expressing FLPE recombinase (pCAGGS-FlpE, Thermo Scientific Open Biosystems, #MES4488) as described[63]. This system involves single copy integration of the transgene downstream of the collagen-1 locus and under control of a doxycycline-inducible promoter. This system enables broad expression in different tissues depending on the expression pattern of the doxycycline-inducible rtTA transgene. Embryonic stem (ES) cells were screened for integration of the transgene by PCR and correctly targeted ES cells were injected into C57Bl/6 blastocysts. Chimeras were crossed to the Ptf1a-Cre strain, and offspring were successively crossed with Rosa26-LSL-rtTA, and LSL-$KRAS^{G12D}$ mice. Compound mutant animals were provided with doxycycline (200 μg/ml) in the drinking water beginning at 4 weeks of age and replaced weekly. A group of control KC and KGC mice that was not provided Dox was euthanized at 12 weeks. Rosa26-LSL-rtTA allele was present in each cohort. Histological examination of the pancreas of these mice revealed a comparable phenotype of focal low grade PanIN (similar to KC mice receiving Dox supplementation; (e.g. see Fig. 1d, e), confirming that the cooperative phenotypes observed in the KGC mice were due to inducible expression of $GNAS^{R201C}$.

Ptf1a-Cre^{ER}, LSL-$KRAS^{G12D}$, $P53^{Lox/Lox}$, and Rosa26-LSL-rtTA and TetO-$GNAS^{R201C}$ strains were intercrossed to obtain $KGPC^{ER}$, KGC^{ER}, KPC^{ER} animals and controls. To activate Cre, 3-week old animals were injected intraperitoneally every other day with 100 mg/kg (body weight) tamoxifen dissolved in corn oil (total 4 doses). Doxycycline (200 μg/ml) was provided in the drinking water beginning at 4 weeks of age. To study the role of $GNAS^{R201C}$ in tumor maintenance, KGC mice were provided Dox supplemented water continually from age 4 weeks (Dox-On) or switched to Dox-free water after tumor detection by palpation at age 8–10 weeks (Dox-Off). The samples were collected at the indicated time points for histological analysis. For abdominal cyst fluid measurement, mice were euthanized at the indicated time points and abdominal cyst fluid was isolated and measured using a 30 ml syringe and 25 g needle.

For subcutaneous tumor studies, 2×10^5 KGC cells or $KGPC^{ER}$ cells (or modified versions of the same) were injected subcutaneously into the lower flank of NOD.CB17-$Prkdc^{scid}$/J mice (6–10 weeks of age)(from Jackson Laboratories, strain #001303). Tumor size was assessed at indicated time points by caliper measurements of length and width and the volume was calculated according to the formula ([length × $width^2$]/2). For orthotopic transplantation studies 2×10^5 tumor cells were prepared in 50% matrigel and injected in a total volume of 30 μl into the tail of the mouse pancreas as described. At the indicated time points the pancreas was harvested and processed for histology and IHC as described in the relevant sections. In experiments involving Dox treatment, Dox supplemented drinking water (200 μg/ml) was first provided one day prior to injection of the tumor cells. For human pancreatic cancer xenograft studies, $7.5–10\times10^5$ cells (in 50% matrigel) were subcutaneously injected into the lower flanks of the NOD.CB17-$Prkdc^{scid}$/J mice (6–10 weeks of age). Tumor growth was followed by caliper measurement until the animals reached humane endpoint criteria.

Histology and immunohistochemical analysis

Tissue samples were fixed overnight in 4% buffered formaldehyde, embedded in paraffin, and then sectioned and stained with haematoxylin and eosin by the MGH Pathology Core. Histological examination was performed by a gastrointestinal cancer pathologist (M.M-K). Immunohistochemistry (IHC) was performed on paraffin-embedded sections (5 μm thickness). After deparaffinization and dehydration, slides were incubated for 10 min with 3 % H_2O_2 at room temperature to block endogenous peroxidase activity. Specimens were brought to the boil in 10 mM sodium citrate buffer (pH 6.0, 5 min, pressure cooker) for antigen retrieval. Slides were blocked for 1 hour in TBS-0.05 % Tween 20 (Fisher Scientific)- 1 drop per 1 ml of Protein Block (Dako X0909) and incubated with primary antibody for 1 hour at room temperature. Primary antibodies were diluted with PBS-Protein Block (1 drop/ml) as follows; anti-MUC1 1:100, anti-MUC2 1:50, anti-MUC5AC 1:100, anti-CK19 1:50, anti-CDX2 1:500, anti-PCNA 1:5000, anti-phospho-(Ser/Thr) PKA substrate 1:200. Specimens were reacted for 30 min with the MACH2 HRP-Polymer reagent combined with secondary antibodies. Slides were then washed with PBS and stained for peroxidase for 1–2 min with the Betazoid DAB Chromogen reagent, washed with water and counterstained with haematoxylin, and mounted from xylene. For Alcian Blue staining, after deparaffinization and dehydration, specimens were rinsed with 3 % acetic acid and then incubated for 20 min with 1% Alcian Blue in 3% acetic acid. Stained slides were photographed with an Olympus DP72 microscope. For quantification of PCNA and phospho-PKA substrate by IHC, % of positively stained IPMN epithelial cell nuclei was counted automatically using ImageJ software (NIH; http://rsb.info.nih.gov/ij). Quantification of mucin-producing IPMN epithelial cells was performed by manually counting % IPMN epithelial cells with Alcian Blue-positive cytoplasm. For quantification of papillary lesions, the % of the total neoplastic ductal area exhibiting papillary structures was assessed using haematoxylin and eosin stained slides.

Isolation and culture of primary tumor cells

Murine pancreatic tumor cells were derived from the following GEM models (KGC: [$KRAS^{G12D/+}$; Rosa26-LSL-$rtTA^{Lox/+}$, TetO-$GNAS^{R201C}$, Ptf1a-Cre]; KGPC: [Ptf1a-Cre^{ER} $KRAS^{G12D/+}$; Rosa26-LSL-$rtTA^{Lox/+}$, TetO-$GNAS^{R201C}$; $p53^{Lox/+}$]; KPC: [Pdx1-Cre; $KRAS^{G12D/+}$; $p53^{Lox/+}$]; KIC: [Pdx1-Cre; $KRAS^{G12D/+}$; $CDKN2A^{Lox/+}$]; KPIC: [Pdx1-Cre; $KRAS^{G12D/+}$; $p53^{Lox/+}$;$p16^{+/-}$]. Tumor tissues were collected in ice cold 20 mL DMEM with 1X Antibiotic-Antimycotic. A transection of the tumor tissue was taken for histological verification and the rest was washed twice with 10 mL HBSS and then minced aseptically with a razor blade on a 10-cm dish. The minced tissue was digested in a small flask for 1 hour on a bench-top stirrer with 2.6 U Liberase DH in 10 mL DMEM containing 1X Antibiotic-Antimycotic at 37 °C. 10 mL tissue homogenates were transferred to a 50 mL falcon tube and centrifuged at 1,000 rpm, 5 min, 4 °C. The pellet was then washed with HBSS 2–3 times by centrifugation. A 100 μm strainer was used to removed undigested large tissue debris. The flow-through was centrifuged at 1,200 rpm for 5 minutes, and the pellet was resuspended with full duct media (DMEM:F12, 5 mg/ml Glucose, 1.22 mg/ml nicotinamide, 5 nM 3,3,5-tri-iodo-L-thyronine, 1 μM Dexamethasone, 5 ml/L ITS+, 1X Pen/Strep, 20 ng/ml mouse EGF, 5% NuSerum IV and 25 μg/ml bovine pituitary extract) with Rho-associated protein kinase (ROCK) inhibitor (10 μg/ml)) and plated on irradiated feeder

cells. Media was supplemented with 200 ng/ml doxycycline. The frozen cells were thawed on feeder layer with ROCK inhibitor and grown as organoids in matrigel or collagen matrix as described unless otherwise stated. For viral infections primary cells were plated in feeder or laminin-coated multi-well plates and infected by spinoculation. KGC^{shp53} cells were initially generated by infecting KGC cells with the LMS sh-p53 retrovirus. PDA cell lines derived from KGC^{shp53} cells used for in vitro studies were generated as follows: KGC^{shp53} cells were injected subcutaneously in NOD.CB17-$Prkdc^{scid}$/J mice. Using the above methods, tumor cultures were subsequently isolated from invasive regions (histologically verified as PDA by analysis of adjacent tissue). The PDA phenotype was subsequently confirmed by re-injection of the cells into NOD.CB17-$Prkdc^{scid}$/J mice.

Human PDA cell lines—1473-2-AMK, 1108-2C926, 1319-3-NE, 1925 2-BHG and 950-5-BLK cells were isolated from patient derived xenografts (PDXs) from MGH pancreatic tumor bank. All study participants provided IRB-approved informed consent for their medical records and tissue samples to be used in this study. Patient clinical data was entered into a de-identified clinical database allowing for the anonymous analysis of demographic, clinical and pathological variables. PDXs were processed as described above and 2D cultures were established in 10% FBS, 1% Pen-strep DMEM-F12. PL45, YAPC, PANC-1 and PaTu-8889T PDA cells are from ATCC repository and were maintained in the same media. The absence of mycoplasma contamination of all the cell lines used in the study was verified by routine testing with LookOut Mycoplasma PCR Kit (Sigma, MP0035).

Generation of SIK CRISPR knockout (KO) cells—Two distinct sets of oligonucleotides encoding gRNAs against mouse Sik1-3 (g1 and g2) were cloned into pLenti-CRISPRV2 (Supplementary Table 1 shows sequences). gRNA against GFP (GFP g1) was used as control[64]. SIK KO KGC cells [Sik (1–3) g1 and Sik (1–3) g2] were generated by combining equal amounts of lentiviruses from each set of gRNAs. Control KGC cells were generated by infection with a comparable amount of GFP g1 viruses. Cells were selected with 5 μg/ml puromycin. Each engineered line was passaged an equal number of times. To verify the efficiency of the gRNAs, polyclonal cell populations were analyzed with immunoblot blot and qRT PCR.

Three-dimensional (3D) organoid assays

Primary low passage (<passage 5) murine tumor cell lines were thawed onto a feeder layer (irradiated or mitomycin C-treated Swiss 3T3 mouse embryonic fibroblasts) on laminin coated plates. Cells were grown in duct media to 30–40% confluence and then trypsinized and passed through a 40 μm filter. For 3D growth assays, both collagen-embedded and matrigel-embedded conditions were tested and yielded comparable results. Collagen-embedding[65] was selected as the primary system due to both ease of handling and lower cost. For all 3D growth assays, 500–1000 viable cells were embedded in collagen in 48-well plates except for IC50 assays, which employed 100–250 cells/well in 96 well plates. In brief, a 1:3.1 vol/vol of duct media containing collagen (Nutragen bovine collagen I, 6.0 mg ml^{-1}) base layer was prepared in multi-well cell culture plates and solidified in a 37 °C humidified incubator. Ice-cold cell suspension/collagen solution 1:8 (vol/vol) was seeded onto the solidified base layer and allowed to solidify. Pharmacologic agents used in the different

experiments were subsequently added in duct media onto the top of the gel and were replaced every two days. Organoid growth was quantified with CyQUANT NF measured after 5–10 days. Two methods were used to quantify organoid growth. 1) At day 5–10 after seeding, the number organoids of ≥ 200 μM were counted under microscope. For IC50 studies and experiments employing organoids with differing morphology, CyQUANT NF (ThermoFisher Scientific) was used to assess growth using a fluorescence assay for DNA content. Both the methods generated comparable results in side-by-side tests. For selected experiments, including the ± Dox, ± FSK, ± SIK inhibitor, and ± shCpt1a studies, replicate studies were performed using 3D matrigel-based cultures in the same media conditions, and gave identical results to those obtained using collagen cultures. For molecular analyses of 3D cultures (proteomics, immunoblots, RNA-seq, qRT-PCR), organoids were grown on a base layer of matrigel in duct media containing diluted (2%) matrigel.

Sphere culture assay—Sphere culture media was prepared in DMEM/F12 medium pen-strep (1%), B27 (20 μl/ml), human EGF (20 ng/ml) and basic FGF (20 ng/ml). Single cell suspension of human cells were seeded in 24 well poly-HEMA coated non-adherent plates in 4% matrigel sphere culture media ± drugs. Spent media was removed by careful aspiration and fresh media ± drugs were added in every two days. After 8–10 days spheres were collected from individual wells, trypsinized in eppendorf tubes and the growth was measured with CyQUANT reagent.

Protein isolation and immunoblotting

Organoids were grown in 3D matrigel cultures. 4–6 days after seeding, ice cold PBS harvesting buffer containing EDTA (5 mM), $NaVO_4$ (1mM), NaF (1.5 mM) with protease inhibitor (1x) was added to organoids, which were then gently dissociated by pipetting and transferred to 15 ml Falcon tubes. Wells were washed with the same buffer and a total of 10 ml of harvesting buffer containing matrigel and organoids was dissolved with a rotary shaker for 1 hr at 4 °C. The tubes were centrifuged for 10 min at 1000 rpm at 4 °C to collect the organoids. The pellet was transferred to a 1.5 mL Eppendorf tube and washed twice with harvesting buffer without EDTA. Cells or organoid pellets were lysed in ice-cold RIPA lysis buffer (150 mM NaCl, 20 mM Tris (pH 7.5), 1 mM EDTA, 1 mM EGTA, 1% Triton X-100, 1% sodium deoxycholate, one tablet of EDTA-free protease inhibitors (per 25 ml) with sonication. Similarly, snap-frozen tissue samples were homogenized in ice-cold RIPA lysis buffer by Fisher scientific PowerGen 125 homogenizer. Samples were clarified by centrifugation and protein content measured using BCA protein assay kit (Thermo Scientific). 10–15 μg protein was resolved on 8–15% SDS-PAGE gels and transferred onto PVDF membranes (GE Healthcare Life Sciences, Pittsburgh, PA). Membranes were blocked in Tris-buffered saline (TBS) containing 5% non-fat dry milk and 0.1% Tween 20 (TBS-T), prior to incubation with primary antibody overnight at 4°C. The membranes were then washed with TBS-T followed by exposure to the appropriate horseradish peroxidase-conjugated secondary antibody for 1 hour and visualized on Kodak X-ray film using the enhanced chemiluminescence (ECL) detection system (Thermo Scientific).

Quantitative RT-PCR

Total cellular RNA was extracted using RNeasy Mini Kit (Qiagen) from 3D organoid culture. Genomic DNA decontamination and reverse transcription were performed in two steps from 1 μg of total RNA using the QuantiTect Reverse Transcription Kit (Qiagen, #205310) according to the manufacturer's instructions. Quantitative RT-PCR was performed with FastStart Universal SYBR Green (Roche) in a Lightcycler 480 (Roche). PCR reactions were performed in triplicate and the relative amount of cDNA was calculated by the comparative CT method using the actin or 18s RNA sequences as a control. The primer sequences were shown in Supplementary Table 1.

Gene Expression Profiling

For RNA-sequencing (RNA-seq) studies, total RNA was isolated in duplicate from two independent KGC lines (A and B) grown in 3D culture with doxycycline supplementation. RNAseq library preparation and sequencing were performed by the Tufts University Genomics Core Facility. RNA samples were prepared using Illumina TruSeq RNA Sample Preparation Kit v2 and sequenced using an Illumina HiSeq 2500 sequencer, generating 50-bp single-end reads. Data was processed using a standard RNA-seq pipeline that used Tophat2 to align the reads to mm9, and the Cufflinks suite to calculate FPKM values.

Multiplexed mass spectrometry-based quantitative proteomics

For proteomics, KGC organoids (two independent lines) were grown in matrigel ± Dox in a 6-well format, harvested as described in the protein isolation section, and snap frozen. Samples were processed and subjected to multiplexed quantitative proteomics analysis using tandem-mass tag (TMT) reagents and the SPS-MS3 method on an Orbitrap Fusion mass spectrometer as described in ref[66].

Gene Set Enrichment Analysis (GSEA)

GSEA[67] was used to analyze the enrichment of functional gene groups among differentially expressed proteins identified in the proteomics analysis of KGC cells grown ± Dox. For each pair of Dox+ and Dox− cells, we calculated the log fold ratio of protein expression averaged across replicates, ranked all detected proteins by this ratio, and applied the GSEA pre-ranked enrichment module to determine significantly enriched GO, KEGG and REACTOME gene sets. The GSEA was run with default settings. P values are calculated based on 1000 permutations. FDR are adjusted for multiple hypothesis testing, and NES are calculated as described[67].

Lipidomic analysis

LC-MS experiments for non-polar metabolites were performed using a KCG organoid line in triplicate for the +Dox and -Dox conditions. All the reagents for lipidomics samples were prepared in LC/MS-grade water. To generate each replicate sample, the 3D organoids from two wells of a 6-well plate were pooled and washed with wash buffer (as described for protein samples) and lipid factions were collected by methanol-chloroform extraction as follows: The organoid pellets were washed with cold 0.9% NaCl. 600 μl of LC/MS-grade methanol at −20°C were added to the tube. Then 300 μl of LC/MS-grade water and 400 μl of

HPLC-grade chloroform (without amylenes) were added to the tubes. The tubes were vortexed for 10 min and then centrifuged at max speed for 10 min at 4°C. After phase separation the bottom layer was collected carefully. The extract was dried in a speed vac and stored at −80°C until analysis. LC-MS/MS-based lipidomic experiments and data analyses were performed as described[68]. The data were normalized to the total number of cells in the organoids from replicate wells.

Polar metabolite profiling

For polar metabolite profiling[69], 2 million cells cultivated on laminin-coated plates with growth factor-reduced duct media were harvested as 5 replicates and flash-frozen. Cell pellets were extracted in 40:40:20 acetonitrile/methanol/water including 10 nM D3-15N-serine as internal standard. Insoluble debris was separated with centrifugation at 13,000 rpm for 10 min. Aliquots of extracts were then injected into an Agilent 6460 or 6430 QQQ-LC/MS/MS. Separation of metabolites was achieved using normal-phase chromatography with a Luna 5 mm NH_2 column (Phenomenex) using a mobile phase (Buffer A, acetonitrile, followed with Buffer B, 95:5 water/acetonitrile) with the modifiers 0.1% formic acid or 0.2% ammonium hydroxide with 50 mM ammonium acetate for positive and negative ionization mode, respectively. Each run used the same flow: 100% A at 0.2 mL/min for 5 min, followed by a gradient starting at 0% B linearly increasing to 100% B in 15 min with a flow rate of 0.7 mL/min, succeeded by an isocratic gradient of 100% B for 5 min at 0.7 mL/min before equilibrating for 5 min with 0% B at 0.7 mL/min. The ion counts were normalized to the total cell number.

MS analysis was performed via an electrospray ionization (ESI) source on an Agilent 6430 or 6460 QQQ LC-MS/MS (Agilent Technologies). The capillary voltage was set to 3.0 kV, and the fragmentor voltage to 100 V. The drying gas temperature was 350°C, flow rate was 10 l/min, and nebulizer pressure was 35 psi. Metabolites were identified by SRM of the transition from precursor to product ions at associated optimized collision energies and retention times as previously described[69]. Metabolites were quantified by integrating the area under the curve, and then normalized to internal standard values.

Fatty acid oxidation (FAO) rate measurement

Fatty acid measurements were adapted from published methods[70]. In brief, cells were cultured in laminin-coated 6-well dishes and incubated overnight in growth factor-reduced duct media (duct media lacking EGF and containing 2.5 ml/L ITS) containing 60 μM oleic acid-BSA and 2 mM carnitine. The next day, the cells were washed and incubated for 4 hours in fresh media supplemented with [1-^{14}C]oleic acid (0.5 μCi) for 4 hours. The media was transferred to a microfuge tube containing Whatman filter paper saturated with phenylethylamine. The reaction was then terminated by adding with 3 M perchloric acid and the tube was closed. The ^{14}CO2 resulting from oxidized fatty acids was captured on the saturated filter paper for 1 hr at room temperature. The radioactivity was measured by scintillation counting and was normalized to total protein content.

Neutral lipid imaging

KGC cells were grown in growth factor-reduced duct media ± Dox on laminin-coated chamber slides until confluent. Cells were incubated with BODIPY dye (10 μg/ml) for 20 minutes. The wells were washed thoroughly with HBSS. Coverslips were then mounted and slides were immediately used for fluorescence imaging. Fluorescence was calculated by image J software.

Cyclic AMP (cAMP) and Acetyl-CoA measurements

cAMP was measured using the Cyclic AMP Assay Kit (4339; Cell Signaling Technology) in KGC cells were grown on laminin-coated plates as above. Acetyl-CoA in Extended Data Fig. 8k was measured using the PicoProbe Acetyl-CoA Fluorometric Assay Kit (K317-100; Biovision). All assays were done according to the manufacturers' protocols.

Statistics and reproducibility

In all cases results are expressed as mean ± standard deviation (s.d.) or mean ± standard error of mean (s.e.m). Significance was analyzed using 2-tailed Student's *t* test where a p value of less than 0.05 was considered statistically significant. Kaplan-Meier curves were analyzed by log-rank test. All statistical calculations were performed by Prism6 software (GraphPad Software, Inc, USA). No samples or animals were excluded from analysis and sample sizes were not predetermined. Animals were randomized in experiments in KGC mice comparing sustained Dox exposure and Dox withdrawal. Also, additional control studies comparing KGC mice provided Dox at 4 weeks versus those that never received Dox were also randomized in a similar manner. Further randomization for both studies involved allocation of females and males into each study condition. All the Immunoblots and IHC were performed two times and generated similar results. For all other experiments the number of biological replicates is indicated in the figure legends.

Data availability

The proteomics data have been deposited in MassIVE proteomics data depository (https://massive.ucsd.edu/) with accession number MSV000082305. The RNA-seq data have been deposited in the NCBI GEO database with accession number GSE114348. The lipidomic and polar metabolite data can be accessed under DOI 10.6084/m9.figshare.6182501 and 10.6084/m9.figshare.6182513 form Figshare repository (https://figshare.com). Source data for Fig. 1, 3–7 and supplementary Fig. 3–7 are provided in Supplementary Table 2. Unprocessed immunoblot scans are presented in Supplementary Fig. 8. All other data supporting the findings of this study are available from the corresponding author on reasonable request.

Supplementary Material

Refer to Web version on PubMed Central for supplementary material.

Acknowledgments

We thank L. Ellisen, R. Mostoslavsky, Filippos Kottakis and other members of the Bardeesy laboratory for helpful suggestions throughout the course of this project and critical reading of the manuscript. We thank C. Wright for

Ptf1a-Cre and Ptf1a-Cre^{ER}, D. Tuveson and T. Jacks for LSL-Kras^{G12D} and A. Berns for P53$^{Lox/Lox}$ animal strains, Nathanael Gray for SIK inhibitors, Sarah Boukhali and Antoine Escudier for experimental support and Mark Keibler for initial help with metabolomics analysis. N.B. holds the Gallagher Endowed Chair in Gastrointestinal Cancer Research and received support from the Granara-Skerry Trust, the Linda J. Verville Foundation, the Begg Family, and grants from the Fibrolamellar Cancer Foundation and the NIH (P01 CA117969-07, R01 CA133557-05, P50CA1270003). K.C.P. is supported by a post-doctoral fellowship from Department of Defense, USA (W81XWH-16-1-0285). K.C.P., Y.M. and N.B. are fellows of the Andrew L. Warshaw Institute for Pancreatic Cancer at Massachusetts General Hospital.

References

1. O'Hayre M, et al. The emerging mutational landscape of G proteins and G-protein-coupled receptors in cancer. Nat Rev Cancer. 2013; 13:412–424. DOI: 10.1038/nrc3521 [PubMed: 23640210]
2. Sassone-Corsi P. The cyclic AMP pathway. Cold Spring Harb Perspect Biol. 2012; 4
3. Rosciglione S, Theriault C, Boily MO, Paquette M, Lavoie C. Galphas regulates the post-endocytic sorting of G protein-coupled receptors. Nat Commun. 2014; 5:4556. [PubMed: 25089012]
4. Drelon C, et al. PKA inhibits WNT signalling in adrenal cortex zonation and prevents malignant tumour development. Nat Commun. 2016; 7:12751. [PubMed: 27624192]
5. He X, et al. The G protein alpha subunit Galphas is a tumor suppressor in Sonic hedgehog-driven medulloblastoma. Nat Med. 2014; 20:1035–1042. DOI: 10.1038/nm.3666 [PubMed: 25150496]
6. Iglesias-Bartolome R, et al. Inactivation of a Galpha(s)-PKA tumour suppressor pathway in skin stem cells initiates basal-cell carcinogenesis. Nat Cell Biol. 2015; 17:793–803. DOI: 10.1038/ncb3164 [PubMed: 25961504]
7. Pattabiraman DR, et al. Activation of PKA leads to mesenchymal-to-epithelial transition and loss of tumor-initiating ability. Science. 2016; 351:aad3680. [PubMed: 26941323]
8. Xing F, et al. The Anti-Warburg Effect Elicited by the cAMP-PGC1alpha Pathway Drives Differentiation of Glioblastoma Cells into Astrocytes. Cell Rep. 2017; 18:468–481. DOI: 10.1016/j.celrep.2016.12.037 [PubMed: 28076790]
9. Wu J, et al. Recurrent GNAS mutations define an unexpected pathway for pancreatic cyst development. Sci Transl Med. 2011; 3:92ra66.
10. Amato E, et al. Targeted next-generation sequencing of cancer genes dissects the molecular profiles of intraductal papillary neoplasms of the pancreas. J Pathol. 2014; 233:217–227. DOI: 10.1002/path.4344 [PubMed: 24604757]
11. Witkiewicz AK, et al. Whole-exome sequencing of pancreatic cancer defines genetic diversity and therapeutic targets. Nat Commun. 2015; 6:6744. [PubMed: 25855536]
12. Bailey P, et al. Genomic analyses identify molecular subtypes of pancreatic cancer. Nature. 2016; 531:47–52. DOI: 10.1038/nature16965 [PubMed: 26909576]
13. Zehir A, et al. Mutational landscape of metastatic cancer revealed from prospective clinical sequencing of 10,000 patients. Nat Med. 2017; 23:703–713. DOI: 10.1038/nm.4333 [PubMed: 28481359]
14. Innamorati G, Valenti MT, Giacomello L, Carbonare L, Bassi C. GNAS Mutations: Drivers or Co-Pilots? Yet, Promising Diagnostic Biomarkers. Trends in Cancer. 2016; 2:282–285. [PubMed: 28741526]
15. Patra KC, Bardeesy N, Mizukami Y. Diversity of Precursor Lesions For Pancreatic Cancer: The Genetics and Biology of Intraductal Papillary Mucinous Neoplasm. Clin Transl Gastroenterol. 2017; 8:e86. [PubMed: 28383565]
16. Cancer Genome Atlas Research Network. Electronic address, a. a. d. h. e. & Cancer Genome Atlas Research, N. Integrated Genomic Characterization of Pancreatic Ductal Adenocarcinoma. Cancer Cell. 2017; 32:185–203 e113. DOI: 10.1016/j.ccell.2017.07.007 [PubMed: 28810144]
17. Aguirre AJ, et al. Activated Kras and Ink4a/Arf deficiency cooperate to produce metastatic pancreatic ductal adenocarcinoma. Genes Dev. 2003; 17:3112–3126. DOI: 10.1101/gad.1158703 [PubMed: 14681207]

18. Farrell JJ, Fernandez-del Castillo C. Pancreatic cystic neoplasms: management and unanswered questions. Gastroenterology. 2013; 144:1303–1315. DOI: 10.1053/j.gastro.2013.01.073 [PubMed: 23622140]
19. Castellone MD, Teramoto H, Williams BO, Druey KM, Gutkind JS. Prostaglandin E2 promotes colon cancer cell growth through a Gs-axin-beta-catenin signaling axis. Science. 2005; 310:1504–1510. DOI: 10.1126/science.1116221 [PubMed: 16293724]
20. Wu J, et al. Inhibition of the EGF-activated MAP kinase signaling pathway by adenosine 3′,5′-monophosphate. Science. 1993; 262:1065–1069. [PubMed: 7694366]
21. Altarejos JY, Montminy M. CREB and the CRTC co-activators: sensors for hormonal and metabolic signals. Nat Rev Mol Cell Biol. 2011; 12:141–151. DOI: 10.1038/nrm3072 [PubMed: 21346730]
22. Yu FX, et al. Regulation of the Hippo-YAP pathway by G-protein-coupled receptor signaling. Cell. 2012; 150:780–791. DOI: 10.1016/j.cell.2012.06.037 [PubMed: 22863277]
23. Cheng H, et al. SIK1 couples LKB1 to p53-dependent anoikis and suppresses metastasis. Sci Signal. 2009; 2:ra35. [PubMed: 19622832]
24. Wehr MC, et al. Salt-inducible kinases regulate growth through the Hippo signalling pathway in Drosophila. Nat Cell Biol. 2013; 15:61–71. DOI: 10.1038/ncb2658 [PubMed: 23263283]
25. Miranda F, et al. Salt-Inducible Kinase 2 Couples Ovarian Cancer Cell Metabolism with Survival at the Adipocyte-Rich Metastatic Niche. Cancer Cell. 2016; 30:273–289. DOI: 10.1016/j.ccell.2016.06.020 [PubMed: 27478041]
26. Patel K, et al. The LKB1-salt-inducible kinase pathway functions as a key gluconeogenic suppressor in the liver. Nat Commun. 2014; 5:4535. [PubMed: 25088745]
27. Sonntag T, Vaughan JM, Montminy M. 14-3-3 proteins mediate inhibitory effects of cAMP on salt-inducible kinases (SIKs). FEBS J. 2017
28. Clark K, et al. Phosphorylation of CRTC3 by the salt-inducible kinases controls the interconversion of classically activated and regulatory macrophages. Proc Natl Acad Sci U S A. 2012; 109:16986–16991. DOI: 10.1073/pnas.1215450109 [PubMed: 23033494]
29. Zechner R, et al. FAT SIGNALS--lipases and lipolysis in lipid metabolism and signaling. Cell Metab. 2012; 15:279–291. DOI: 10.1016/j.cmet.2011.12.018 [PubMed: 22405066]
30. Park J, et al. SIK2 is critical in the regulation of lipid homeostasis and adipogenesis in vivo. Diabetes. 2014; 63:3659–3673. DOI: 10.2337/db13-1423 [PubMed: 24898145]
31. Wang B, et al. A hormone-dependent module regulating energy balance. Cell. 2011; 145:596–606. DOI: 10.1016/j.cell.2011.04.013 [PubMed: 21565616]
32. Bricambert J, et al. Salt-inducible kinase 2 links transcriptional coactivator p300 phosphorylation to the prevention of ChREBP-dependent hepatic steatosis in mice. J Clin Invest. 2010; 120:4316–4331. DOI: 10.1172/JCI41624 [PubMed: 21084751]
33. Benjamin DI, et al. Ether lipid generating enzyme AGPS alters the balance of structural and signaling lipids to fuel cancer pathogenicity. Proc Natl Acad Sci U S A. 2013; 110:14912–14917. DOI: 10.1073/pnas.1310894110 [PubMed: 23980144]
34. Lodhi IJ, Semenkovich CF. Peroxisomes: a nexus for lipid metabolism and cellular signaling. Cell Metab. 2014; 19:380–392. DOI: 10.1016/j.cmet.2014.01.002 [PubMed: 24508507]
35. Li YQ, et al. Gsalpha deficiency in adipose tissue improves glucose metabolism and insulin sensitivity without an effect on body weight. Proc Natl Acad Sci U S A. 2016; 113:446–451. DOI: 10.1073/pnas.1517142113 [PubMed: 26712027]
36. Louie SM, Roberts LS, Mulvihill MM, Luo K, Nomura DK. Cancer cells incorporate and remodel exogenous palmitate into structural and oncogenic signaling lipids. Biochim Biophys Acta. 2013; 1831:1566–1572. DOI: 10.1016/j.bbalip.2013.07.008 [PubMed: 23872477]
37. Menendez JA, Lupu R. Fatty acid synthase and the lipogenic phenotype in cancer pathogenesis. Nat Rev Cancer. 2007; 7:763–777. DOI: 10.1038/nrc2222 [PubMed: 17882277]
38. Currie E, Schulze A, Zechner R, Walther TC, Farese RV Jr. Cellular fatty acid metabolism and cancer. Cell Metab. 2013; 18:153–161. DOI: 10.1016/j.cmet.2013.05.017 [PubMed: 23791484]
39. Padanad MS, et al. Fatty Acid Oxidation Mediated by Acyl-CoA Synthetase Long Chain 3 Is Required for Mutant KRAS Lung Tumorigenesis. Cell Rep. 2016; 16:1614–1628. DOI: 10.1016/j.celrep.2016.07.009 [PubMed: 27477280]

40. Nomura DK, et al. Monoacylglycerol lipase regulates a fatty acid network that promotes cancer pathogenesis. Cell. 2010; 140:49–61. DOI: 10.1016/j.cell.2009.11.027 [PubMed: 20079333]
41. Viale A, et al. Oncogene ablation-resistant pancreatic cancer cells depend on mitochondrial function. Nature. 2014; 514:628–632. DOI: 10.1038/nature13611 [PubMed: 25119024]
42. Lim JH, et al. Oleic acid stimulates complete oxidation of fatty acids through protein kinase A-dependent activation of SIRT1-PGC1alpha complex. J Biol Chem. 2013; 288:7117–7126. DOI: 10.1074/jbc.M112.415729 [PubMed: 23329830]
43. Gerhart-Hines Z, et al. The cAMP/PKA pathway rapidly activates SIRT1 to promote fatty acid oxidation independently of changes in NAD(+). Mol Cell. 2011; 44:851–863. DOI: 10.1016/j.molcel.2011.12.005 [PubMed: 22195961]
44. Wilderman A, et al. Proteomic and Metabolic Analyses of S49 Lymphoma Cells Reveal Novel Regulation of Mitochondria by cAMP and Protein Kinase A. J Biol Chem. 2015; 290:22274–22286. DOI: 10.1074/jbc.M115.658153 [PubMed: 26203188]
45. Ying H, et al. Oncogenic Kras maintains pancreatic tumors through regulation of anabolic glucose metabolism. Cell. 2012; 149:656–670. DOI: 10.1016/j.cell.2012.01.058 [PubMed: 22541435]
46. Dominguez E, et al. Integrated phenotypic and activity-based profiling links Ces3 to obesity and diabetes. Nat Chem Biol. 2014; 10:113–121. DOI: 10.1038/nchembio.1429 [PubMed: 24362705]
47. Mino-Kenudson M, et al. Prognosis of invasive intraductal papillary mucinous neoplasm depends on histological and precursor epithelial subtypes. Gut. 2011; 60:1712–1720. DOI: 10.1136/gut.2010.232272 [PubMed: 21508421]
48. Honeyman JN, et al. Detection of a recurrent DNAJB1-PRKACA chimeric transcript in fibrolamellar hepatocellular carcinoma. Science. 2014; 343:1010–1014. DOI: 10.1126/science.1249484 [PubMed: 24578576]
49. Shackelford DB, Shaw RJ. The LKB1-AMPK pathway: metabolism and growth control in tumour suppression. Nat Rev Cancer. 2009; 9:563–575. DOI: 10.1038/nrc2676 [PubMed: 19629071]
50. Lodish M, Stratakis CA. A genetic and molecular update on adrenocortical causes of Cushing syndrome. Nat Rev Endocrinol. 2016; 12:255–262. DOI: 10.1038/nrendo.2016.24 [PubMed: 26965378]
51. Gaujoux S, et al. Hepatobiliary and Pancreatic neoplasms in patients with McCune-Albright syndrome. J Clin Endocrinol Metab. 2014; 99:E97–101. DOI: 10.1210/jc.2013-1823 [PubMed: 24170100]
52. Bossis I, et al. Protein kinase A and its role in human neoplasia: the Carney complex paradigm. Endocr Relat Cancer. 2004; 11:265–280. [PubMed: 15163302]
53. Taki K, et al. GNAS(R201H) and Kras(G12D) cooperate to promote murine pancreatic tumorigenesis recapitulating human intraductal papillary mucinous neoplasm. Oncogene. 2016; 35:2407–2412. DOI: 10.1038/onc.2015.294 [PubMed: 26257060]
54. von Figura G, et al. The chromatin regulator Brg1 suppresses formation of intraductal papillary mucinous neoplasm and pancreatic ductal adenocarcinoma. Nat Cell Biol. 2014; 16:255–267. DOI: 10.1038/ncb2916 [PubMed: 24561622]
55. Collins MA, et al. Oncogenic Kras is required for both the initiation and maintenance of pancreatic cancer in mice. J Clin Invest. 2012; 122:639–653. DOI: 10.1172/JCI59227 [PubMed: 22232209]
56. Wang YY, et al. Mammary adipocytes stimulate breast cancer invasion through metabolic remodeling of tumor cells. JCI Insight. 2017; 2:e87489. [PubMed: 28239646]
57. Caro P, et al. Metabolic signatures uncover distinct targets in molecular subsets of diffuse large B cell lymphoma. Cancer Cell. 2012; 22:547–560. DOI: 10.1016/j.ccr.2012.08.014 [PubMed: 23079663]
58. Prentki M, Madiraju SR. Glycerolipid/free fatty acid cycle and islet beta-cell function in health, obesity and diabetes. Mol Cell Endocrinol. 2012; 353:88–100. DOI: 10.1016/j.mce.2011.11.004 [PubMed: 22108437]
59. Schug ZT, Vande Voorde J, Gottlieb E. The metabolic fate of acetate in cancer. Nat Rev Cancer. 2016; 16:708–717. DOI: 10.1038/nrc.2016.87 [PubMed: 27562461]
60. Hauser AS, Attwood MM, Rask-Andersen M, Schioth HB, Gloriam DE. Trends in GPCR drug discovery: new agents, targets and indications. Nat Rev Drug Discov. 2017; 16:829–842. DOI: 10.1038/nrd.2017.178 [PubMed: 29075003]

61. Dickins RA, et al. Probing tumor phenotypes using stable and regulated synthetic microRNA precursors. Nat Genet. 2005; 37:1289–1295. DOI: 10.1038/ng1651 [PubMed: 16200064]

62. Kawaguchi Y, et al. The role of the transcriptional regulator Ptf1a in converting intestinal to pancreatic progenitors. Nat Genet. 2002; 32:128–134. DOI: 10.1038/ng959 [PubMed: 12185368]

63. Beard C, Hochedlinger K, Plath K, Wutz A, Jaenisch R. Efficient method to generate single-copy transgenic mice by site-specific integration in embryonic stem cells. Genesis. 2006; 44:23–28. DOI: 10.1002/gene.20180 [PubMed: 16400644]

64. Sanjana NE, Shalem O, Zhang F. Improved vectors and genome-wide libraries for CRISPR screening. Nature methods. 2014; 11:783–784. DOI: 10.1038/nmeth.3047 [PubMed: 25075903]

65. Reichert M, et al. Isolation, culture and genetic manipulation of mouse pancreatic ductal cells. Nature protocols. 2013; 8:1354–1365. DOI: 10.1038/nprot.2013.079 [PubMed: 23787893]

66. Lapek JD Jr, et al. Detection of dysregulated protein-association networks by high-throughput proteomics predicts cancer vulnerabilities. Nat Biotechnol. 2017; 35:983–989. DOI: 10.1038/nbt.3955 [PubMed: 28892078]

67. Subramanian A, et al. Gene set enrichment analysis: a knowledge-based approach for interpreting genome-wide expression profiles. Proc Natl Acad Sci U S A. 2005; 102:15545–15550. DOI: 10.1073/pnas.0506580102 [PubMed: 16199517]

68. Smulan LJ, et al. Cholesterol-Independent SREBP-1 Maturation Is Linked to ARF1 Inactivation. Cell reports. 2016; 16:9–18. DOI: 10.1016/j.celrep.2016.05.086 [PubMed: 27320911]

69. Louie SM, et al. GSTP1 Is a Driver of Triple-Negative Breast Cancer Cell Metabolism and Pathogenicity. Cell Chem Biol. 2016; 23:567–578. DOI: 10.1016/j.chembiol.2016.03.017 [PubMed: 27185638]

70. Huynh FK, Green MF, Koves TR, Hirschey MD. Measurement of fatty acid oxidation rates in animal tissues and cell lines. Methods Enzymol. 2014; 542:391–405. DOI: 10.1016/B978-0-12-416618-9.00020-0 [PubMed: 24862277]

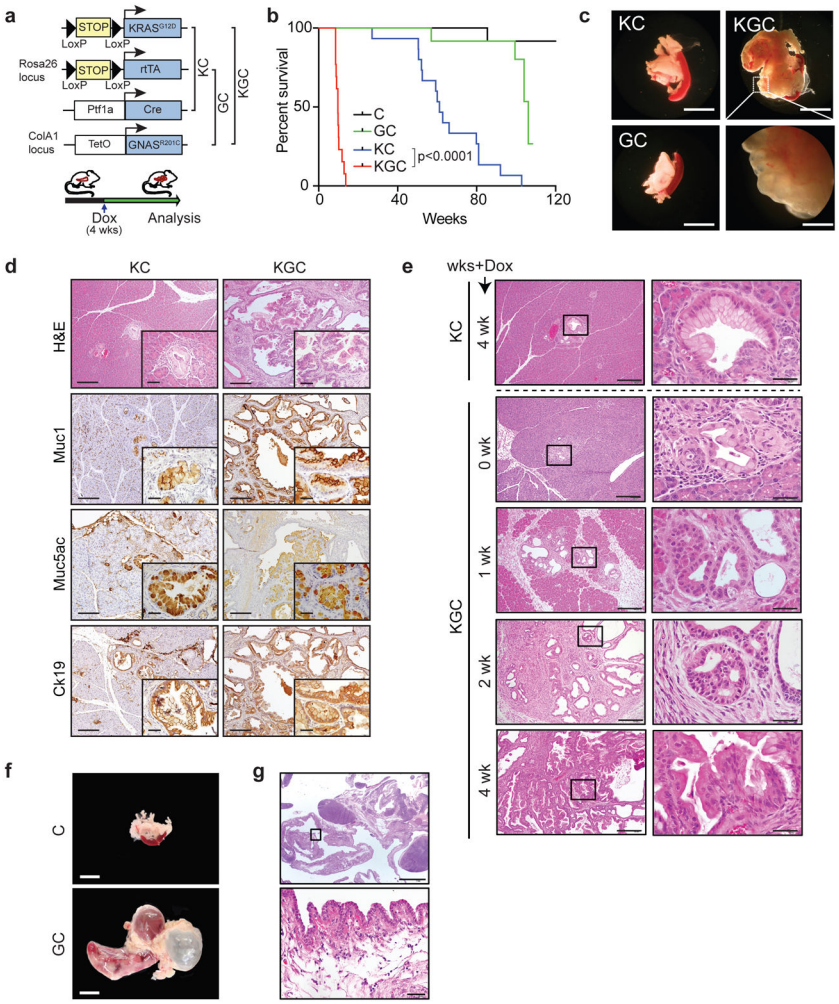

Figure 1. Pancreas-specific GNAS^{R201C} and KRAS^{G12D} mutations cooperate to promote IPMNs

a, Schematic of mouse strains. **b,** Kaplan-Meier analysis for time until tumor progression necessitated euthanasia (KGC: N=13, KC: N=15, GC: N=12, C: N=14; N represents mouse numbers]). Kaplan-Meier curves were analyzed by log-rank test. $p< 0.05$ was considered statistically significant. **c,** Photographs depicting pancreata from 12-week old mice of the indicated genotypes. Representative of 10 mice/group. **d,** H&E stained sections (*top panels*) and IHC stained sections for the indicated markers (*lower panels*). Representative of 10 mice/group for H&E and 3 mice/group for IHC. (d) *inset:* higher magnification. **e,** H&E staining of KC and KGC pancreata at the indicated time points (representative of 3 mice/group). *Right panels:* higher magnification of the boxed regions. **f,** Gross photograph of the pancreas from a representative GC mouse and control mouse at age 61 weeks. **g,** H&E stained section of the GC pancreas at age 61 weeks. The background in (f) was edited in Photoshop for presentation purposes. Data in f and g are representative of 4 GC mice. Scale bars: (c) 1 cm, (d) 200 μm, inset 40 μm, (e) 200 μm *left* and 40 μm *right*, (f) 1 cm, (g) 2 mm *upper*, 40 μm *lower*. Source data are provided in Supplementary Table 2.

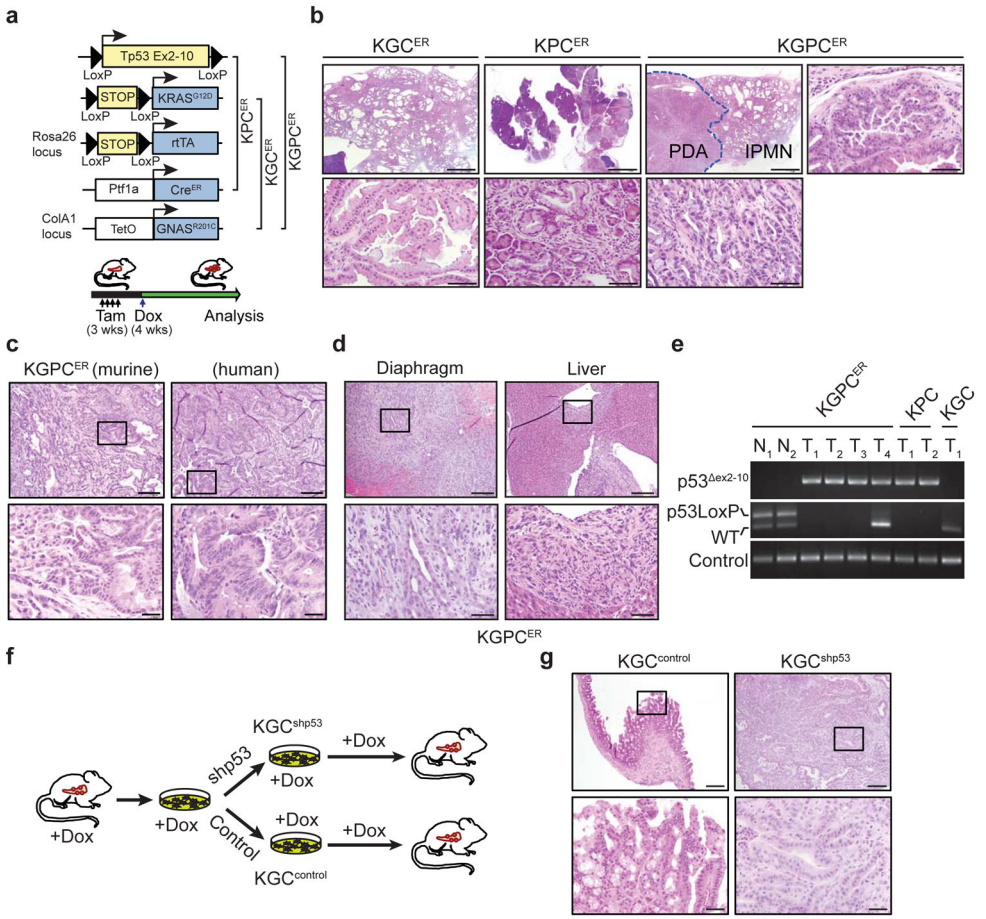

Figure 2. Tp53 loss facilitates progression of GNAS^{R201C}-KRAS^{G12D} IPMN to PDA

a, Schematic of mouse strains to examine interactions between GNAS^{R201C}, KRAS^{G12D} and heterozygous Tp53 inactivation in the pancreas. **b,** H&E staining of pancreata from the indicated genotypes following 25–28 weeks of Dox supplementation. *Bottom panels and far right*: higher magnification views. Data are representative of 8 KGC^{ER}, 5 KPC^{ER}, and 8 KGPC^{ER} mice. **c,** H&E stained section of a PDA from a KGPC^{ER} mouse (representative of 8 KGPC^{ER} mice). A human IPMN-associated PDA (tubular carcinoma) is shown for comparison. **d,** H&E stained sections revealing distant spread of PDA in KGPC^{ER} mice to the diaphragm and liver (observed in 2/8 mice). **e,** PCR analysis showing loss of the wild type *Tp53* allele in 3/4 PDAs from the KGPC^{ER} model. DNA was isolated from low-passage KGPC^{ER} tumor cells. The controls are normal DNA from KGPC^{ER} mice, PDA DNA from the *Tp53*-deficient KPC GEM model, and IPMN DNA from the KGC model. N, Normal; T, Tumor. Data are representative of two independent PCR analyses. **f,** Schematic of development of KGC^{shp53} model. **g,** H&E stained images of pancreatic tumors formed 6 weeks after orthotopic injection of KGC^{Control} and KGC^{shp53} cultures. KGC^{Control} cells produce IPMNs whereas KGC ^{shp53} cells result in invasive PDA contiguous with IPMN lesions (representative of 6/group). The boxed regions in (c, d and g) are shown in higher magnification in the lower panels. Scale bars: (b) 2 mm for first three upper panels, otherwise 40 μm; (c, d and g) 200 μm *upper*, 40 μm *lower*.

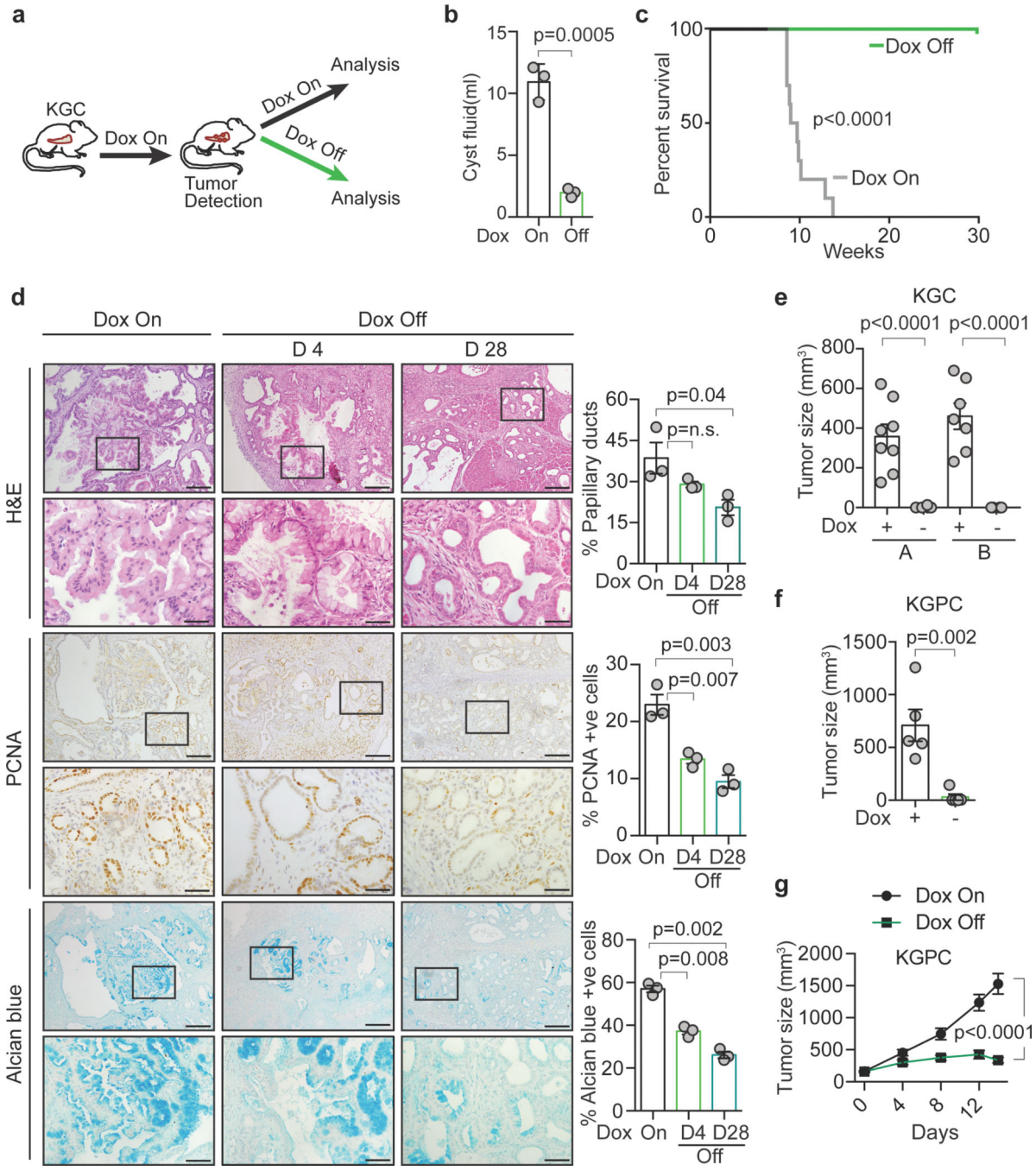

Figure 3. GNAS^{R201C} is critical for pancreatic tumor maintenance

a, Approach to study GNAS^{R201C} tumor maintenance function. **b,** Measurement of pancreatic abdominal cyst fluid volume upon necropsy at end-stage (Dox On group) or after 4 weeks following Dox removal (Dox Off group). N=3 mice per group. **c,** Kaplan-Meier analysis of time until tumor progression necessitated euthanasia. Dox On (N=10 mice; included in the cohort depicted in (Fig. 1b), Dox Off (N=12 mice). Kaplan-Meier curves were analyzed by log-rank test. $p< 0.05$ was considered statistically significant. **d,** Pancreatic tumors from KGC mice isolated at end-stage (Dox On group) or at the indicated time points

following Dox withdrawal were analyzed by (d) H&E staining (*top panels*), IHC staining for PCNA (*middle panels*), and Alcian blue staining for acidic mucins *(bottom panels*). Lower panels for each stain: magnification of boxed region. Representative of 3 mice/group. *Right*: charts quantifying histologic and staining data. **e, f,** Volume of tumors in SCID mice ± Dox supplementation isolated 6 weeks after subcutaneous injection of (**e**) KGC organoids (N=8 and 7 mice/group for organoid lines A and B, respectively) and (**f**) $KGPC^{ER}$ organoids (N= 5 mice/group). **g**) Mice injected subcutaneously with $KGPC^{ER}$ organoids were provided Dox until tumors reached ~62.5 mm^3 in volume. Animals were then randomized into +Dox and -Dox conditions and analyzed for serial changes in tumor volume. (N=10 tumors/ group). Scale bars in (d) are 200 μm (upper panels) and 40 μm (lower panels). Significance was analysed using two-tailed Student's t-test. $p< 0.05$ was considered statistically significant. Error bars: (b, d–g: ± s.e.m.). Source data are provided in Supplementary Table 2.

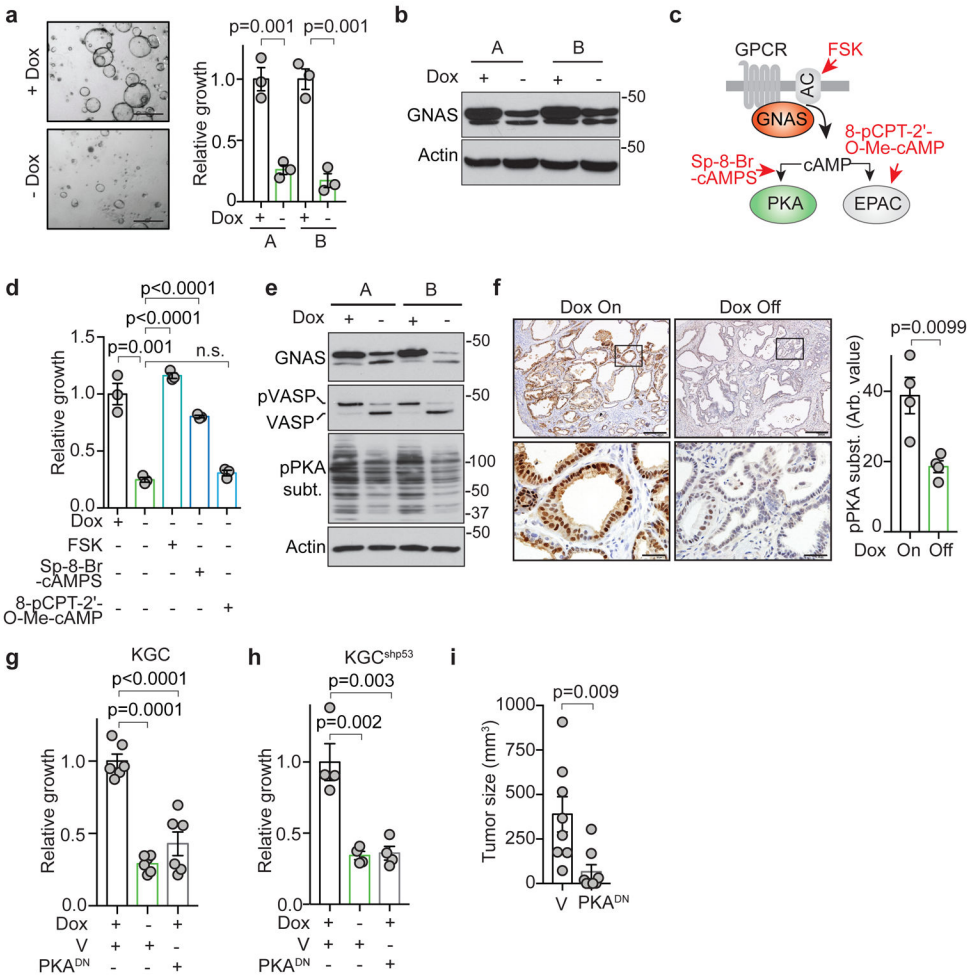

Figure 4. GNAS^{R201C} supports pancreatic tumor growth via cAMP-PKA signaling

a, Organoids cultures established from two independent KGC tumors (lines A and B) were tested for *in vitro* growth ± Dox (200 ng/ml) after 7 days. *Left*, gross photos, *Graph*: quantification. **b,** Immunoblot showing GNAS regulation in KGC cells. **c,** Schematic of GNAS signaling and targets of agonists. **d,** Quantification of KGC organoid growth ± Dox and ± the indicated agonists. **e,** Immunoblot showing PKA regulation in KGC cells as determined by VASP mobility shift (*i.e.* PKA-phosphorylated VASP), and by anti-phospho-PKA substrate antibody. **f,** IHC staining using anti-phospho-PKA substrate antibody in KGC tumors in mice +Dox or following Dox withdrawal. *Bottom*: higher magnification of boxed regions. Data are quantified in the chart (right). **g, h,** Growth of KGC (**g**) and KGC ^{shp53} (**h**) organoids expressing empty vector (V) or PKA^{DN} cultured ± Dox. **i,** Tumor volume at 6 weeks following subcutaneous injection of KGC organoids expressing empty vector (V) or PKA^{DN}. Scale bars: (a) 500 μm (f) *upper* panel 200 μm, *lower* 40 μm. a, d: N=3 independent biological replicates; b, e: immunoblots were performed two times with similar results; f: N=4 mice/group; g: N=6 independent biological replicates; h: N=4 independent biological replicates; I: N=8 tumors/group. Error bars: (a, d, f–i: ± s.e.m.). Significance was analysed using two-tailed Student's t-test. $p< 0.05$ was considered statistically significant. Source data

are provided in Supplementary Table 2. Original scans of the immunoblots are shown in Supplementary Fig. 8.

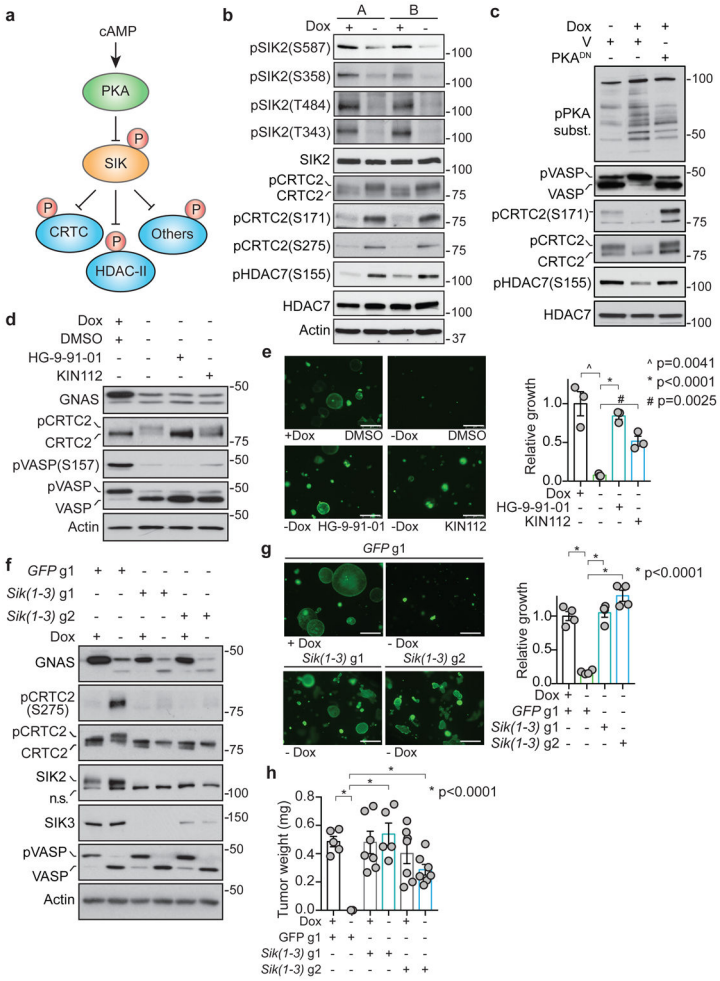

Figure 5. The SIK kinases are critical targets of oncogenic GNAS-PKA signaling in pancreatic tumors

a, Schematic of PKA-SIK signaling. **b,** Immunoblots of lysates from KGC organoids grown ± Dox, demonstrating $GNAS^{R201C}$-mediated regulation of phosphorylation of SIK2, CRTC2, and HDAC7. Note: CRTC2 phosphorylation is indicated by phosphospecific antibodies and mobility shift. **c,** Immunoblot of lysates from the indicated KGC organoids grown ± Dox and expressing empty vector (V) or PKA^{DN}, showing that PKA^{DN} effectively inhibits PKA signaling and activates SIKs. **d, e,** KGC organoids were cultured ± Dox and ± the indicated SIK inhibitor (250 nM) for 7 days. **d,** Immunoblot documenting PKA-SIK signaling changes. CRTC2 phosphorylation is completely blocked by HG-9-91-01 and partially blocked by KIN112. **e,** Organoid growth assessed by fluorescence using the CyQUANT reagent. *Left* photomicrographs of the growth of the organoids; *Right* Quantification. **f–h,** Study of KGC organoids expressing Cas9 and sgRNA against GFP or against *Sik1*, 2, and 3 (two sets of sgRNAs targeting different regions of each *Sik* homolog were used). *Sik1-3* gene editing resulted in (**f**) loss of SIK2 and SIK3 protein and defective CRTC2 phosphorylation following Dox withdrawal, (**g**) rescue of proliferation following Dox withdrawal (quantified at right), and (**h**) rescue of subcutaneous tumor growth *in vivo* in the absence of Dox supplementation. Scale bars: (e, g) 750 μm. Immunoblots in b–d and f

were performed two times with similar results. e, g, N=3 and 4 independent biological replicates, respectively. h. GFPg1+Dox (N=5), GFPg1-Dox (N=7), Sik(1–3)g1+Dox (N=7), Sik(1–3)g1-Dox (N=5) Sik(1–3)g2+Dox (N=7), Sik(1–3)g2-Dox (N=7); N represents number of tumors. Error bars: (e, g, h: ± s.e.m.). Significance was analysed using two-tailed Student's t-test. $p < 0.05$ was considered statistically significant. Source data are provided in Supplementary Table 2. Original scans of the immunoblots are shown in Supplementary Fig. 8.

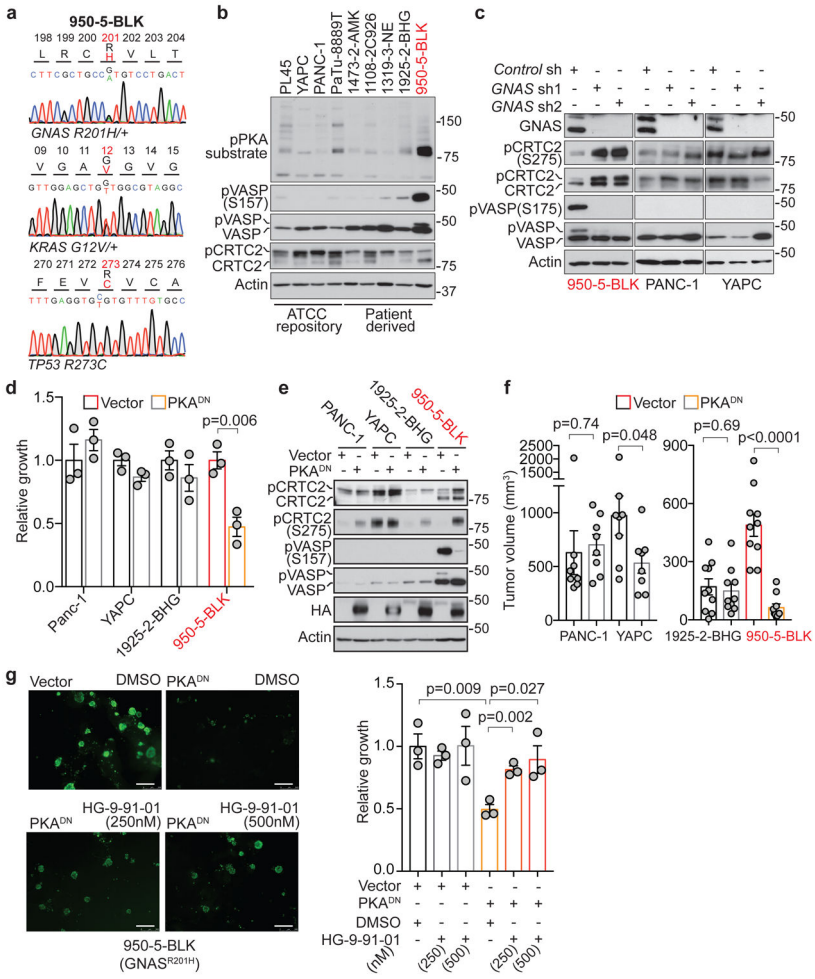

Figure 6. The GNAS-PKA-SIK axis drives growth of human patient-derived PDA cells harboring concurrent GNAS, KRAS, and Tp53 mutations

a, Sequencing chromatograms of 950-5-BLK cells, derived from a human PDA patient, showing $GNAS^{R201H}$, $KRAS^{G12V}$, and $TP53^{R273C}$ mutations. Sequencing was performed from two independent DNA isolations and PCR reactions. **b,** Immunoblot of a series of PDA cell lines, including those from the ATCC repository and newly established patient-derived lines. The single GNAS mutant line, 950-5-BLK shows highest PKA activity and uniquely exhibits CRTC2 primarily in its unphosphorylated form. **c,** Immunoblot of the indicated PDA cell lines expressing two different shRNAs against GNAS or control shGFP. GNAS knockdown blocks PKA signaling and specifically activates SIK-mediated CRTC2 phosphorylation in 950-5-BLK cells. **d–f,** The indicated human PDA cell lines were engineered to express PKA^{DN} or empty vector and (**d**) tested for relative growth as matrigel spheroid cultures, (**e**) subjected to immunoblot analysis for activity of PKA and SIK, and (**f**) tested for tumorigenicity upon subcutaneous injection in SCID mice. **g,** Growth as spheroids of 950-5-BLK cells expressing PKA^{DN} treated with increasing amounts of the indicated pan-SIK inhibitor (HG-9-91-01). Cells transduced with empty vector are shown as controls. The data are graphed at the right (the inhibitor-treated vector-expressing cells are not represented in photomicrographs). Scale bars: (g) 500 μm. Immunoblots in b, c and e were

performed two times with similar results. d, g: N=3 independent biological replicates. f: PANC-1 and YAPC (N=8 tumors/group) and 1925-2-BHG and 950-5-BLK (N=10 tumors/group). Error bars: (d, f and g: ± s.e.m.). Significance was analysed using two-tailed Student's t-test. $p < 0.05$ was considered statistically significant. Source data are provided in Supplementary Table 2. Original scans of the immunoblots are shown in Supplementary Fig. 8.

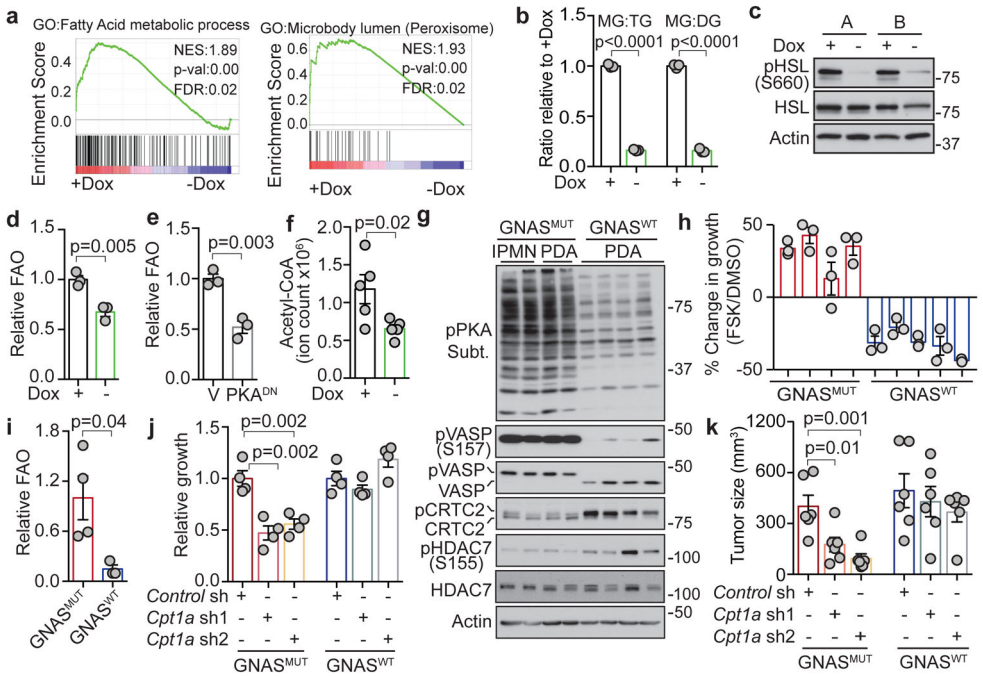

Figure 7. Mutant GNAS reprograms lipid metabolism in pancreatic tumor cells

a, GSEA was performed using quantitative proteomics data from two independent KGC organoid lines grown ± Dox. GNAS^{R021C} positively regulates fatty acid metabolism and peroxisomal gene sets as defined in the Biological Process (BP) and Cellular Compartment (CC) categories from the Gene Ontology (GO) database. Data are from two independent quantitative proteomics experiments with the following number of replicates/condition: Experiment #1: 2 replicates/condition for both organoid lines; Experiment #2: 3 replicates for organoid line A and 2 replicates for organoid line B. p values are calculated based on 1000 permutations and adjusted for multiple hypothesis testing. **b,** KGC organoids grown ± Dox were analysed by global lipidomics. The graph shows that the relative MG:TG ratio and MG:DG ratios are decreased upon Dox withdrawal. **c,** Immunoblot showing GNAS^{R201C}-dependent phosphorylation of HSL (Ser-660) in KGC organoids. **d, e,** Relative FAO rate assessed by $^{14}CO_2$ trap in KGC cultures grown ± Dox (**d**) or +Dox and ± PKA^{DN} (**e**). **f,** Relative acetyl-CoA levels in KGC cultures grown ± Dox, detected by LC-MS. **g,** Immunoblot of organoids from GNAS mutant (KGC; IPMN) and (KGC^{shp53}; PDA) and GNAS WT PDA (KPC, KIC, and KPIC) models (see Methods). **h,** Relative growth of GNAS mutant and WT organoids ± FSK (10 μM). **i,** Relative FAO rates. **j, k,** Impact of Cpt1a knockdown using two different shRNAs on (**j**) organoid growth and (**k**) tumorigenesis upon subcutaneous injection. b, d, e, h: N=3; f: N=5; j; N=4 independent biological replicates; c and g: Immunoblots were performed two times with similar results; i: N=4 cell lines for GNAS^{MUT} and N=3 cell lines for GNAS^{WT}; k: N=6 tumors/group. Error bars: (b, d–f, h–k: ± s.e.m). Significance was analysed using two-tailed Student's t-test. $p< 0.05$ was considered statistically significant. Source data are provided in Supplementary Table 2. Original scans of the immunoblots are shown in Supplementary Fig. 8.